(A New Proposal to Jefferson Lab PAC34)

Measurement of the Neutron Electromagnetic Form Factor Ratio G_E^n/G_M^n at High Q^2

A. Camsonne, E. Chudakov, P. Degtyarenko, J. Gomez,
O. Hansen, D. W. Higinbotham, C. W. de Jager, M. Jones, J. LeRose, R. Michaels, S. Nanda,
A. Saha, V. Sulkosky, B. Wojtsekhowski (spokesperson and contact person), S. Wood
Thomas Jefferson National Accelerator Facility, Newport News, VA 23606

H. Baghdasaryan, G. Cates (spokesperson), D. Day, N. Kalantarians,
R. Lindgren, N. Liyanage, V. Nelyubin[†], B. E. Norum,
S. Riordan (spokesperson), M. Shabestari, W. A. Tobias, K. Wang
University of Virginia, Charlottesville, VA 22901

D. Nikolenko, I. Rachek, Yu. Shestakov
Budker Institute, Novosibirsk, Russia

K. Aniol and D. J. Magaziotis
California State University, Los Angeles, CA 90032

G. B. Franklin, B. Quinn, R. Schumacher
Carnegie Mellon University, Pittsburgh, PA 15213

J. Annand, D. Hamilton, D. Ireland, R. Kaiser, K. Livingston,
I. MacGregor, G. Rosner, B. Seitz
University of Glasgow, Glasgow, Scotland

W. Boeglin, P. Markowitz, J. Reinhold, M. M. Sargsian
Florida International University, Miami, FL 33199

B. Anderson, A.T. Katramatou, G.G. Petratos
Kent State University, Kent, OH 44242

A. Glamazdin
Kharkov Institute of Physics and Technology, Kharkov 310077, Ukraine

W. Bertozzi, S. Gilad
Massachusets Institute of Technology, Cambridge, MA 02139

J. Calarco, W. Hersman, K. Slifer
University of New Hampshire, Durham, NH 03824

M. Khandaker, V. Punjabi
Norfolk State University, Norfolk, VA 23504

B. Vlahovic
North Carolina Central University, Durham, NC 03824

R. Gilman, C. Glashausser, G. Kumbartzki, R. Ransome
Rutgers, The State University of New Jersey, Piscataway, NJ 08854

J. M. Laget, F. Sabatie
CEA Saclay, Gif-sur-Yvette, France

A. Sarty
Saint Mary's University, Nova Scotia, Canada B3H 3C3

R. De Leo, L. Lagamba, S. Marrone, G. Simonetti, E. Nappi, I. Vilardi
INFN Bari and University of Bari, Bari, Italy

V. Bellini, A. Giusa, F. Mammoliti, C. Randieri,
G. Russo, M. L. Sperduto, C. M. Sutera
INFN Catania and University of Catania, Catania, Italy

E. De Sanctis, L. Hovsepyan, M. Mirazita, S. A. Pereira, P. Rossi
INFN, Laboratori Nazionali di Frascati, Frascati, Italy

E. Cisbani, F. Cusanno, S. Frullani, F. Garibaldi,
M. Iodice, M. L. Magliozzi, F. Meddi, G. M. Urciuoli
INFN Rome and gruppo collegato Sanità and University "La Sapienza", Rome, Italy

A. D'Angelo
INFN Rome2 and University "Tor Vergata", Rome, Italy

J. Lichtenstadt, E. Piasetzky, I. Pomerantz, G. Ron
Tel Aviv University, Israel

T. Averett, L. Pentchev, C. Perdrisat
College of William and Mary, Williamsburg, VA 23185

S. Abrahamyan, S. Mayilyan, A. Shahinyan, H. Voskanyan
Yerevan Physics Institute, Yerevan, Armenia

M. Olson
St. Norbert College, De Pere, WI 54115

† on leave from SPNPI of Russian Academy of Sciences, Gatchina, Russia

January 2, 2009

Abstract

We propose a measurement of the electromagnetic form factor ratio of the neutron, G_E^n/G_M^n, at high four–momentum transfer values of Q^2 = 5.0, 6.8, and 10.2 GeV^2 in double polarized semi-exclusive $^3\overrightarrow{\mathrm{He}}(\vec{e},e'n)pp$ scattering in quasi–elastic kinematics by measuring the transverse asymmetry, $A_\perp$, of the cross section. This quantity can then be used to quickly extract the electric form factor, G_E^n, as more precise high Q^2 G_M^n data becomes available.

Results from the recent JLab experiments E93-027, E04-108 for elastic electron-proton scattering, using a recoil polarization technique, show remarkable features for the proton electric form factor at these momentum transfers, whereas no data on G_E^n are available. Our previous measurement of G_E^n in experiment E02-013 provided data up to Q^2 of 3.5 GeV^2, which more than doubles the previously covered Q^2 range.

The recently developed approach for calculations of exclusive reactions in the Q^2-range between 1 and 10 GeV^2 using generalized parton distributions (GPD) relates these elastic form factors and the results from deep inelastic scattering and deeply virtual Compton scattering. Data for G_E^n at high Q^2 are necessary, in particular, to constrain spin-flip GPDs at high momentum transfer.

The experiment utilizes the polarized ^{3}He target and the polarized JLab beam at beam energies of 4.4, 6.6, and 8.8 GeV. The electrons will be detected in the BigBite spectrometer with a new GEM based tracker and the neutrons in an array of scintillators. Because of the high kinetic energy of the neutrons, a high neutron detection efficiency with an excellent background suppression can be achieved. Separation of recoiling protons and neutrons will be performed magnetically.

Within 55 days of beamtime the ratio G_E^n/G_M^n can be measured to an accuracy better than $\Delta(G_E^n/G_M^n)$= 0.20 for these three values of Q^2. With accurate measurements of G_M^n, this would correspond to $\Delta(G_E^n/G_D)$ = 0.07, or $\Delta G_E^n = 3\times10^{-4}$ for our highest Q^2 point. Such a measurement would significantly increase our knowledge about a fundamental property of the neutron in a region where no data are available.

1 Introduction

Knowledge of the neutron electromagnetic form factors, G_E^n and G_M^n, are essential for an understanding of nucleon structure. At non-relativistic momentum transfers, they are the Fourier transforms of the electric charge and magnetic moment distributions, respectively, of the valence and sea quarks inside the neutron. At relativistic energies in the Breit–frame, where the squared three-momentum transfer, $\vec{q}^2$, equals the square of the four-momentum transfer, Q^2, they are related to the Fourier transforms of these distributions. This creates difficulties in the interpretation of the charge distribution in the nucleon rest frame, as the Briet frame is different for each Q^2. An attempt to relate the Briet frame distributions to the rest frame distributions has recently been explored [1].

Recent surprising results on G_E^p, the electric form factor of the proton, from JLab experiments E93-027 and E99-007, utilizing a recoil polarization technique, show that the ratio G_E^p/G_M^p declines sharply as Q^2 increases, and therefore that the electric and magnetic form factors exhibit different Q^2 behavior starting at $Q^2 \approx 1$ GeV^2 [2, 3]. The same mechanisms causing this deviation should also be present in the neutron. It is an intriguing question, how the ratio G_E^n/G_M^n develops in this Q^2 regime, where confinement plays an important role.

Our knowledge of G_E^n at high Q^2 is rather poor compared to the data available on the Sachs form factors of the proton, G_E^p and G_M^p, as well as, but to a lesser extent, on the neutron magnetic form factor G_M^n. The reason is two-fold. First, the net charge of the neutron is zero and G_E^n is therefore a small quantity and second, there are no sufficient free neutron targets on which to perform experiments.

Thermal–neutron scattering from atoms measures very precisely the RMS charge radius related to the slope of $G_E^n(Q^2)$ as $Q^2 \to 0$ [4, 5]. This has been measured to be -0.113 fm^2, and because the net charge of the neutron is zero, it can be thought to consist of a positive core surrounded by a negative cloud. There are a number of physical mechanisms which have been proposed to explain the origin of the neutron's charge distribution. The classical interpretation was in terms of a virtual negatively charged π^- cloud surrounding a positively charged proton core.

Measuring G_E^n in inclusive unpolarized electron scattering is limited in the accuracy of the information it can provide. This is typically performed using the technique of Rosenbluth separation. The Rosenbluth formula is given by

$$\frac{d\sigma}{d\Omega} = \frac{d\sigma}{d\Omega}\Big|_{\text{Mott}} \Big(\frac{G_E^2 + \tau G_M^2}{1+\tau} + 2\tau G_M^2 \tan^2 \frac{\theta}{2} \Big) = \frac{\alpha^2 \cos^2 \frac{\theta}{2}}{4E^2 \sin^4 \frac{\theta}{2}} \frac{E'}{E} \Big(\frac{G_E^2 + \tau G_M^2}{1+\tau} + 2\tau G_M^2 \tan^2 \frac{\theta}{2} \Big), \quad (1)$$

where E is the initial electron energy, E' is the final electron energy, $tau = Q^2/4M^2$ where Q^2 is the four-momentum transfer and M is the mass of the nucleon, and θ is the scattering angle of the electron. By measuring the cross section for several θ at fixed Q^2, the values of G_E and G_M can be separated. Applying this technique for the neutron is very demanding for several reasons. Since $\tau G_M^n \gg G_E^n$, the magnetic form factor dominates the cross section, making the accurate extraction of G_E^n difficult. Additionally, these experiments have to be performed on light nuclei, typically ^{2}H, and the contribution from the proton to the cross section must be subtracted. Furthermore, to extract the neutron information, the deuteron wave functions must be known, and FSI, MEC, IC, and relativistic effects must be included.

Double polarization experiments provide another tool to study G_E^n. By investigating spin observables, the interference between G_E^n and G_M^n enhances the sensitivity of these reactions to

G_E^n. This possibility was already discussed in 1957 by Akhiezer *et al.* [6] and later in 1969 by Dombey [7], and again by Akhiezer and Rekalo [8]. Arnold, Carlson, and Gross suggested studying the reaction $d(\vec{e},e'\vec{n})p$ to determine G_E^n [9]. In 1984 Woloshyn proposed the use of a polarized ^{3}He target to measure G_E^n [10].

Experiments [11, 12, 13, 14] at MAMI were the first to utilize such a target and measured G_E^n at several points up to 0.7 GeV^2. Experiment E02-013 in Hall A used a polarized ^{3}He target to measure G_E^n at four Q^2 points from 1.4 to 3.5 GeV^2. In the last ten years, a variety of double polarization experiments measuring G_E^n have been performed at different facilities: MIT-Bates, NIKHEF, MAMI, and JLAB Halls A and C.

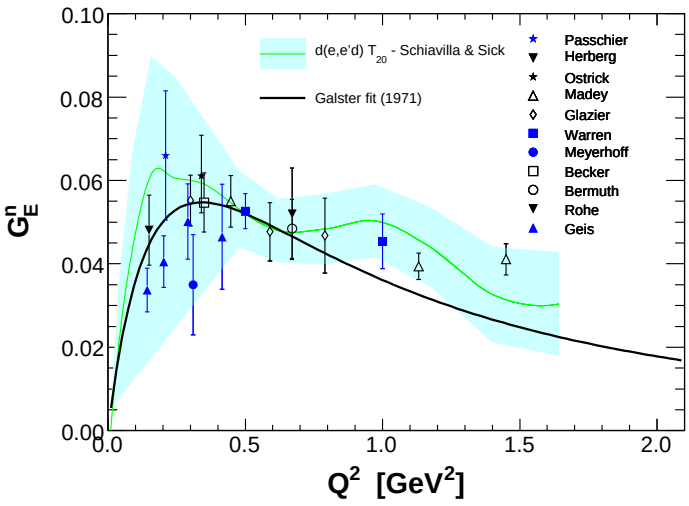

Figure 1: Selected published G_E^nworld data from polarized measurement techniques [11, 12, 13, 14, 15, 16, 17, 18, 19, 20, 21] and G_E^n extracted from the deuteron quadrapole form factor [22]. Also shown is the Galster parameterization [23].

Fig. 1 shows the published results on G_E^n obtained from these types of experiments [11, 12, 13, 14, 15, 16, 17, 18, 19, 20, 21] and G_E^n extracted from the deuteron quadrapole form factor [22]. Also shown is the Galster parameterization, [23], where the form factor of the neutron is given by the curve

$$G_E^n = \frac{-\mu_n \tau}{1+5.6\tau} G_{\rm D}, \tag{2}$$

where $G_{\rm D}$ is the dipole parameterization,

$$G_D = \left(1+\frac{Q^2}{0.71\ {\rm GeV}^2}\right)^{-2}. \tag{3}$$

For moderate Q^2, G_M^n has been well determined by a recent and soon to be published analysis from CLAS [24, 25] and was determined to follow the dipole parameterization quite well, Fig. 2. However, at the time of this writing, there is a lack of precision data above 4.0 GeV^2, which would presently hinder the extraction of G_E^n from the ratio G_E^n/G_M^n. As this data becomes available, G_E^n could be quickly be calculated.

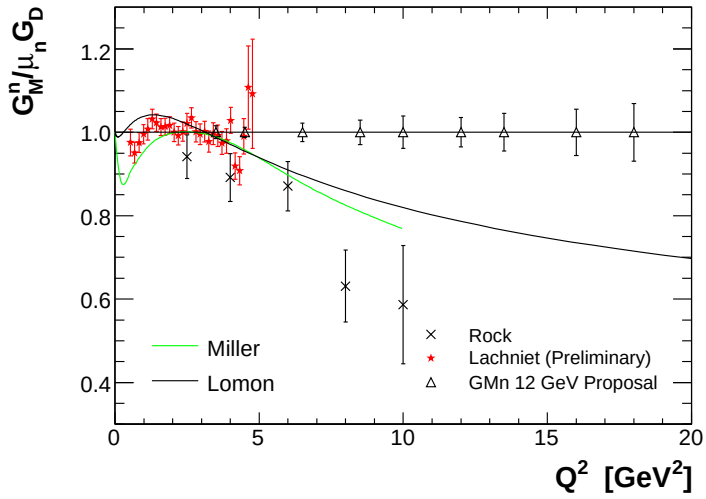

Figure 2: G_M^n data for moderate and high $Q^2$from [24, 25], [26], and a new 12 GeV proposal.

In Fig. 3 are the projected data points from the proposed experiment, preliminary results for E02-013, and the empirical fit from Galster.

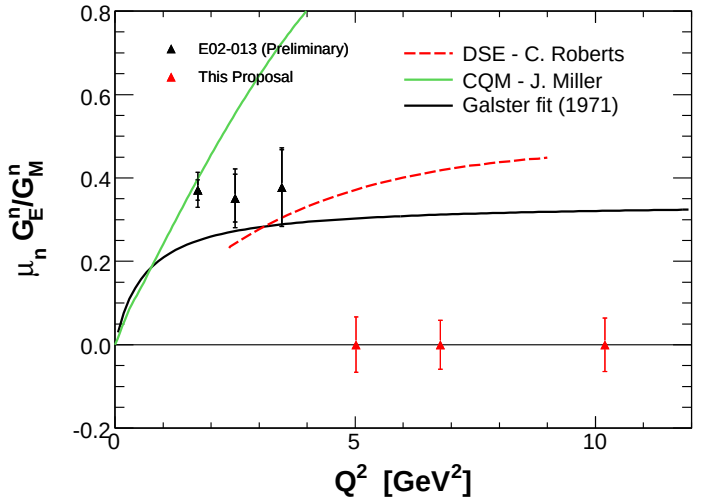

Figure 3: Projected points for this proposal and preliminary results from E02-013.

To address the actual physics interests, we propose to measure G_E^n/G_M^n at Q^2=5.0, 6.8, and 10.2 GeV^2. We expect to achieve a relative statistical uncertainty in $\Delta(G_E^n/G_M^n)$ of 20% or better in each of the three data points in 1385 hours of beamtime. This accuracy is comparable to the precision of the data on the proton, so a direct comparison of neutron and proton form factor data will be possible. In this error estimate, we have assumed that G_E^n follows the Galster parameterization and for G_M^n a parameterization of Kelly [27] was used. At this time, there is no accurate G_E^n data is available from double polarization measurements for Q^2 greater than 3.5 GeV^2. There is also

no other approved experiment at JLab, which is the only laboratory where a double polarization measurement of G_E^n at such high momentum transfers is possible.

The experiment is made possible by two advantages: first, the large acceptance BigBite spectrometer and a neutron detector with an angular acceptance matched to the electron arm results in a large solid angle which cannot be achieved with any of the other standard detectors in Hall A or Hall C; second is the large degree of neutron polarization in the Hall A polarized ^{3}He target, which has a luminosity capability which exceeds that of other polarized targets. The use of the polarized ^{3}He target together with the polarized electron beam allows us to perform a double polarization experiment without the need to use a polarimeter to measure the polarization of the recoiling neutron. Additionally, due to the high momentum of the recoiling neutron, the neutron detector can be built with a very high neutron detection efficiency.

2 Physics Motivation

The nucleon plays the same central role in hadronic physics that the hydrogen atom does in atomic physics and the deuteron in the physics of nuclei. The structure of the nucleon and its general properties, such as charge, magnetic moment, size, mass, and the appropriate form factors, are of fundamental scientific interest. The nucleon is a laboratory for the study of the quark-gluon interaction and both nucleons, the proton and the neutron, need to be explored. At present the proton has been more thoroughly studied at large Q^2 than the neutron. More data on the neutron is essential if we are to make real progress in obtaining a complete description of the quark structure of the nucleon.

Considerable information on the structure of the nucleon has been obtained by using electromagnetic probes via electron scattering. Inclusive deep inelastic scattering (DIS) has been a classical tool with which the partonic structure of the nucleon has been probed. At high Q^2, DIS yields information on the light-cone momentum space distributions of quarks and gluons in the nucleon when viewed through the infinite momentum frame. Many of the experimental foundations of QCD are in fact derived from investigations of various aspects of DIS.

Exclusive processes, on the other hand, such as elastic electron and photon scattering, can provide information on the spatial distribution of the nucleon's constituents, which is parameterized through the elastic nucleon form factors. For photon scattering, only one set of data, obtained at Cornell in 1977 [28], on high energy scattering off the proton at large s, t, and u is available. Experimental studies of elastic electron scattering from both the proton and the neutron were initiated at SLAC and are now being thoroughly performed at Jefferson Lab and other facilities world-wide.

The Dirac form factor, F_1, describes the distribution of electric charge and the Dirac magnetic moment, while the helicity non-conserving Pauli form factor, F_2, describes the distribution of the Pauli magnetic moment; these two form factors are the ingredients of the hadronic current. These currents contain information on the transverse charge distribution for an unpolarized and transversely polarized nucleon, respectively, in the infinite momentum frame [29, 30].

The Sachs form factors, G_E and G_M, the ratio of which will be extracted directly from our data for the neutron, are related to F_1 and F_2 by

$$F_1 = \frac{G_E + \tau G_M}{1+\tau} \text{ and } F_2 = \frac{G_M - G_E}{\kappa(1+\tau)}, \tag{4}$$

where κ is the nucleon anomalous magnetic moment.

The independent determination of G_M^p from the unpolarized ep cross section data has been made up to Q^2 = 8.8 GeV^2 [31]. The extraction of G_M^p from a single cross section measurement to higher Q^2 assumes $\mu_p G_E^p = G_M^p$ [32]; these data are shown in Fig. 4. New data from the GEp-III experiment in Hall C at JLab using polarization transfer to measure G_E^p/G_M^p up to 8.5 GeV^2 is currently under analysis.

In the case of the neutron, new measurements of G_M^n in Hall B [24, 25] are near publication; they will bring the knowledge of this form factor to comparable levels of accuracy to Q^2 = 4.8 GeV^2. For the neutron electric form factor, JLab experiment E02-013 is currently in analysis and will extend the Q^2 range to 3.5 GeV^2.

The PAC15 Workshop on Nucleon and Meson Form Factors and Sum Rules addressed the following scientific questions:

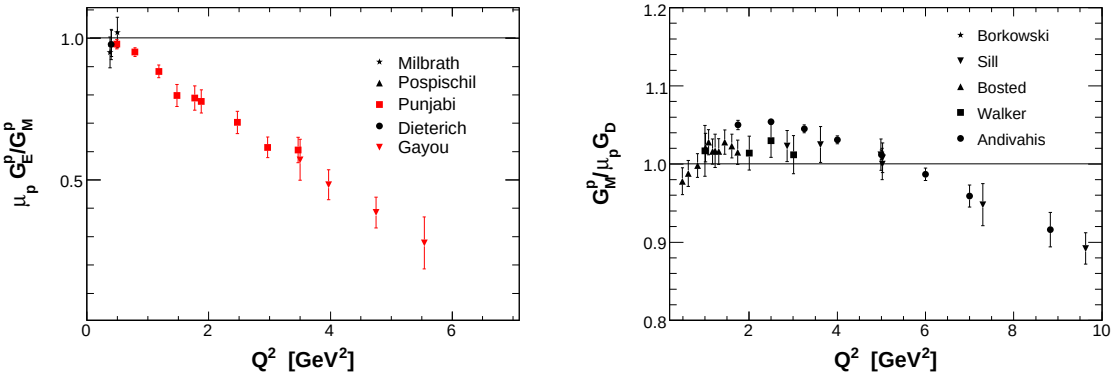

Figure 4: Selected world data for $\mu_p G_E^p/G_M^p$ and for $G_M^p/\mu G_D$.

- What is the role of perturbative QCD in understanding nucleon form factors at high Q^2?
- Can we understand the nucleon as a strongly interacting few-body system?
- Can form factor ratios be calculated in believable QCD-motivated models?
- Can non-forward distributions provide a link between form factors and structure functions?

As we discuss in the following, the measurement of G_E^n at a few GeV^2 proposed here will provide fundamental information needed for answering these questions.

At asymptotically high Q^2, one can apply perturbative QCD (pQCD) to describe the Q^2 dependence of exclusive electron scattering. Early attempts to determine the scaling behavior for F_1 were performed by using a simple dimensional counting rule justified by the inclusion of two gluon exchange processes [33, 34]. A recent calculation by Belitski *et al.* [35] was performed where quark orbital angular momentum was included to determine the behavior for the non-helicity conserving form factor F_2. It was found to logarithmic accuracy that the ratio F_2/F_1 should, at high Q^2, follow the form

$$\frac{F_2}{F_1} \propto \frac{\log^2\left(Q^2/\Lambda^2\right)}{Q^2}, \tag{5}$$

This behavior was found to set in surprisingly early for the proton data for $Q^2 > 2.0$ GeV^2 with $\Lambda \approx 300$ MeV. Using preliminary G_E^n data from E02-013 up to 3.5 GeV^2, this scaling had not yet been observed [36] suggesting pQCD has not yet set in at this range in Q^2. A calculation from ANL utilizing a Poincare invariant truncated Faddeev equation for a quark-diquark system [37] suggests this type of behavior for each of the two nucleons may be expected. For high Q^2, this experiment in conjunction with high Q^2 G_M^n data may be able to observe the onset of this pQCD behavior in the neutron form factors.

Over the years many QCD-inspired models have been developed to describe nucleon electromagnetic form factors at small and intermediate Q^2 values ($Q^2 < 1$–2 GeV^2). While these have provided some insights into the possible origin of the nonperturbative quark structure of the nucleon, ultimately one would like to use experimental form factor data to test the workings of QCD itself. Recently, important developments in QCD phenomenology has been the exploration of the

generalized parton distribution (GPD) formalism [38, 39, 40], which provides model–independent relations between inclusive and exclusive observables. For example, the nucleon elastic form factors F_1 and F_2 are given by the first moments of the GPDs

$$F_1(t) = \sum_q \int_0^1 H^q(x,\xi,t,\mu)dx \text{ and } F_2(t) = \sum_q \int_0^1 E^q(x,\xi,t,\mu)dx, \tag{6}$$

where H^q and E^q are two of the generalized parton distributions, x is the standard Bjorken x, ξ is is the "skewdness" of the reaction (Fig. 5), t is the four-momentum transfered by the electron, μ is a scale parameter necessary from the evolution over Q^2, analogous to DIS parton distributions, and the sum is over all quarks and anti-quarks. These may be accessed through processes such as deeply virtual compton scattering, where the interaction is factorized into a hard part with the virtual photon/photon interactions with an individual quark and a soft part of the residual system where the GPD information is contained, Fig. 5.

Furthermore, as shown earlier by Ji [38], the moments of GPDs can yield information, according to the Angular Momentum Sum Rule, on the contribution to the nucleon spin from quarks and gluons, including both the quark spin and orbital angular momentum.

At present, experimental measurements of GPDs are scarce. Until such data becomes available, work has been done to attempt to parameterize these GPDs, which rely heavily on data from electromagnetic form factors and parton distributions from DIS as constraints [41, 42, 43]. Data at high Q^2 for G_E^n would contribute significantly in the development of these models.

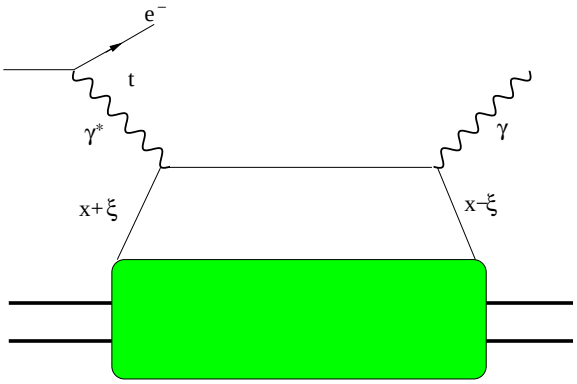

Figure 5: DVCS scattering process which allows access to GPDs.

3 The Double Polarization Method

In the following paragraphs we will briefly summarize the formalism used to describe cross sections and asymmetries obtained in doubly polarized electron scattering experiments. We will mainly follow the approach of [49, 50]. In the Born approximation, the elastic electron nucleon scattering ($e-N$) cross section can be written as a sum of two parts: Σ, which corresponds to the unpolarized elastic differential cross section $d\sigma/d\Omega_e$, and a polarized part Δ, which is only non-zero if the electron is longitudinally polarized (helicity $h = \pm 1$);

$$\sigma_h = \Sigma + h\Delta. \tag{7}$$

The asymmetry A_N for the $e-N$ scattering cross section is defined as

$$A_N = \frac{\sigma_+ - \sigma_-}{\sigma_+ + \sigma_-} = \frac{\Delta}{\Sigma}. \tag{8}$$

The unpolarized $e-N$ cross section Σ for elastic scattering off a free nucleon at rest is given by

$$\Sigma = \left.\frac{d\sigma}{d\Omega}\right|_{\text{Mott}} \frac{E_f}{E_i}\left(\frac{G_E^2 + \tau G_M^2}{1+\tau} + 2\tau G_M^2 \tan^2(\theta/2)\right), \tag{9}$$

with

$$\left.\frac{d\sigma}{d\Omega}\right|_{\text{Mott}} = \frac{\alpha^2 \cos^2\frac{\theta}{2}}{4E_i^2 \sin^4\frac{\theta}{2}} \tag{10}$$

being the Mott cross section, which describes the scattering of a spin one-half particle from a point-like spin one-half target. The polarized part is given by

$$\Delta = -2\left.\frac{d\sigma}{d\Omega}\right|_{\text{Mott}} \frac{E_f}{E_i}\sqrt{\frac{\tau}{1+\tau}}\tan(\theta/2)\left[\sqrt{\tau(1+(1+\tau)\tan^2(\theta/2))}\cos\theta^* G_M^2 + \sin\theta^*\cos\phi^* G_M G_E\right], \tag{11}$$

where θ^* is the polar angle and ϕ^* is the azimuthal angle of the target polarization in the laboratory frame with respect to the axis of the momentum transfer (Fig. 6).

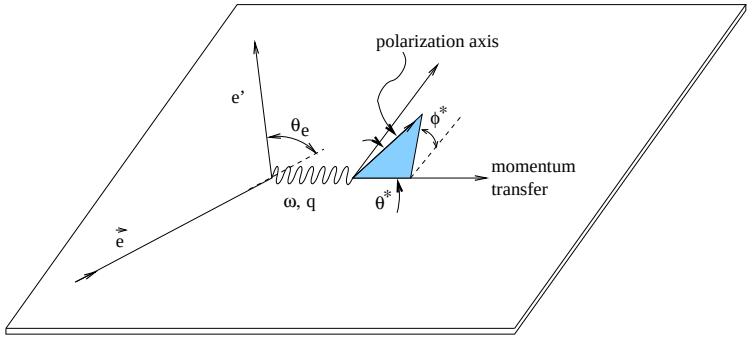

Figure 6: The kinematics of electron scattering from a polarized target.

The measured experimental asymmetry for the $^3\overrightarrow{\text{He}}(\vec{e},e'n)pp$ reaction is reduced compared to this ideal $\vec{n}(\vec{e},e'n)$ reaction due to a number of effects. Limited polarization of the electron beam

$P_{\rm beam}$ and the ^{3}He target, $P_{^3{\rm He}}$, the effective polarization of the neutrons in the ^{3}He target, P_n, the addition of nitrogen in the ^{3}He target, $D_{\rm N_2}$, the dilution from accidental background events, $D_{\rm back}$, contributions from inelastic pion production, D_π, and reductions from nuclear effects, $D_{\rm FSI}$.

At JLab beam polarizations of $P_{\rm beam} = 0.85$ are routinely achieved. The polarized ^{3}He target has been operated at average values of about $P_{\rm He} = 0.50$ during experiment E02-013. Plans to continue to improve the maximum polarization by the polarized ^{3}He target groups are underway, with the expectation of reaching 0.65. The total spin of ^{3}He is mainly carried by the neutron, so a polarized ^{3}He target represents an effective polarized neutron target. As many authors have shown [51, 52, 53, 54, 55, 56, 57], even for a 100% polarized ^{3}He nucleus, the neutron itself has only a polarization of 0.86 ± 0.02. Additionally, the protons in polarized ^{3}He nuclei are not completely unpolarized, but carry a polarization of -0.028 ± 0.004. The presence of nitrogen in the target cell leads to $D_{\rm N_2} \approx 0.94$, and background events lead to $D_{\rm back} = 0.95$ (see Sec. 4.3 and 6). Final state interactions can reduce the asymmetry by a factor of 0.9$\sim$0.95. Contributions from inelastic pion production may change the asymmetry by approximately 20%, and needs to be evaluated from experimental data.

The measured asymmetry from the neutron can now be expressed as

$$A_{\rm exp} = P_{\rm beam} P_{^3{\rm He}} P_n D_{\rm N_2} D_\pi D_{\rm FSI} A_{\rm phys} \tag{12}$$

with

$$\begin{aligned} A_{\rm phys} &= -\frac{2\sqrt{\tau(\tau+1)}\tan(\theta/2) G_E^n G_M^n \sin\theta^* \cos\phi^*}{(G_E^n)^2 + (G_M^n)^2(\tau + 2\tau(1+\tau)\tan^2(\theta/2))} \\ &\quad -\frac{2\tau\sqrt{1+\tau+(1+\tau)^2\tan^2(\theta/2)}\tan(\theta/2)(G_M^n)^2\cos\theta^*}{(G_E^n)^2 + (G_M^n)^2(\tau + 2\tau(1+\tau)\tan^2(\theta/2))} \,. \end{aligned} \tag{13}$$

By aligning the target spin perpendicular to the momentum transfer, one gets the perpendicular asymmetry:

$$A_\perp = -\frac{G_E^n}{G_M^n} \frac{2\sqrt{\tau(\tau+1)}\tan(\theta/2)}{(G_E^n/G_M^n)^2 + (\tau + 2\tau(1+\tau)\tan^2(\theta/2))} \,. \tag{14}$$

Because $(G_E^n/G_M^n)^2$ is small compared to the second term of the denominator in our kinematics, G_E^n is nearly proportional to $A_\perp$. To extract G_E^n out of this ratio, knowledge of G_M^n is necessary. At present the $Q^2 = 10$ GeV^2 G_M^n data [26] would introduce a 20% error to G_E^n, which is near the sum of all other contributions to the uncertainty. The accurate extraction of G_E^n will have to rely on future high Q^2 G_M^n measurements.

Due to the large acceptance of the BigBite spectrometer and the neutron detector array, the perpendicular spin alignment can only be made for part of the acceptance, and longitudinal contributions to the asymmetry have to be taken into account

$$A_\parallel = -\frac{2\tau\sqrt{1+\tau+(1+\tau)^2\tan^2(\theta/2)}\tan(\theta/2)}{(G_E^n/G_M^n)^2 + (\tau + 2\tau(1+\tau)\tan^2(\theta/2)).} \tag{15}$$

With the ability to reconstruct the scattering angles and the momentum transfer, and a well measured magnetic holding field for the target, these corrections are under control.

The above discussion described scattering from a free nucleon. The general case of electron scattering from a bound nucleon was also analyzed by Donnelly [50]. Additional components, which appear in the cross section, are nulled when the cross section is integrated over the azimuthal angle of the nucleon momentum relative to the direction of the momentum transfer and the electron scattering plane. The remaining differences between the case of a free and a bound nucleon will be addressed in Sec. 5.

4 Experimental Setup

As illustrated in Fig. 7, this experiment will study the scattering of longitudinally polarized electrons from a transversely polarized ^{3}He target held in a vacuum. The scattered electron will be detected in the BigBite spectrometer with a modified electron detector stack. A dipole magnet acquired from Brookhaven, 48D48, which we dub BigBen, will deflect recoiling protons and a scintillator array, matched to the BigBite acceptance, will be used to detect the recoiling nucleon.

We will also make use of enhanced target cells to ensure optimal performance during the experiment. The BigBite spectrometer GEM chambers are presently in the design and prototyping phase and the gas Cerenkov currently being commissioned for the Transversity experiment, E06-010/E06-011, and d_2^n, E06-014. The calorimeter configuration will remain identical to that used in earlier experiments.

The neutron detector will use existing and new neutron bars, but will have a design very similar to that used in the previous G_E^n experiment, E02-013. The following subsections describe in more detail the modifications and additions necessary to carry out this experiment.

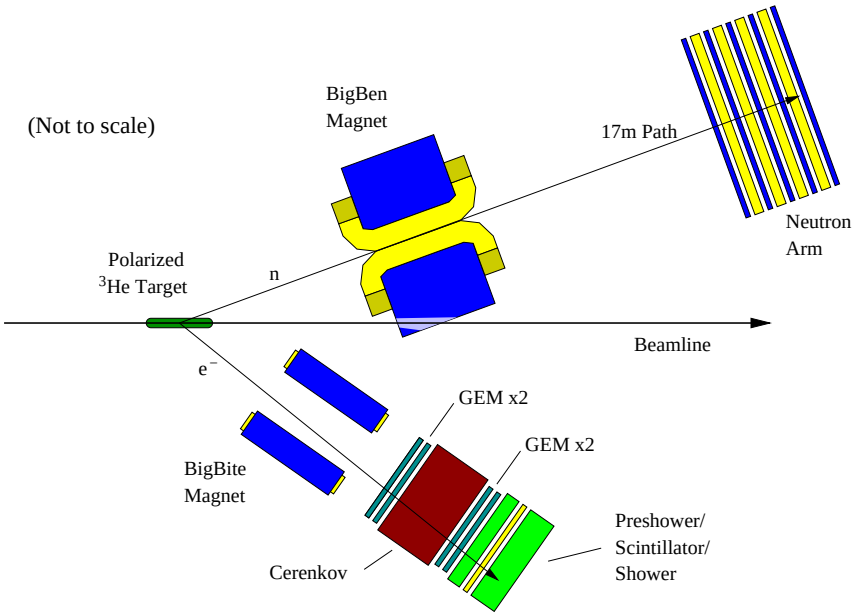

Figure 7: Layout of the experimental setup (not to scale).

4.1 The CEBAF Polarized Beam

In our rate calculations we have assumed 60μA of beam with 85% polarization. The beam polarization will mainly be measured with the Hall A Møller polarimeter, which is able to measure this quantity with a systematic uncertainty of 3%. This uncertainty can be improved by calibrating the Møller polarimeter against the Compton polarimeter, which itself has only a systematic uncertainty of 1.4%.

4.2 The Polarized ^{3}He Target

The polarized target for GEN-II will use the technique of spin-exchange optical pumping, the same technique that was used for GEN-I (E02-013), as well as the other polarized ^{3}He experiments conducted in Hall A. At first glance, the proposed target for GEN-II appears quite ambitious. The target we describe below will provide an effective luminosity roughly 15-16 times larger than was the case during GEN-I, and 7–8 times larger than the ^{3}He experiments that are running at the time of this writing. The fundamental advancements that will provide the improved luminosity, however, have already been largely demonstrated. What distinguishes the GEN-II target from previous polarized ^{3}He targets is that it takes better advantage of the progress that has been made in recent years.

There are five distinct factors that play a key role in making the GEN-II target possible:

1. The introduction of alkali-hybrid mixtures to greatly increase the efficiency with which the angular momentum of photons is transferred to ^{3}He nuclei.
2. The introduction of greatly improved diagnostics that permit not just polarimetry of the ^{3}He, but also polarimetry of the alkali-metal vapors as well as the direct measurement of the alkali-vapor number densities.
3. The advent of commercially available line-narrowed high-power diode-laser arrays.
4. The recognition of the presence of a poorly understood, but measurable, ^{3}He spin-relaxation mechanism that can be characterized by something that has come to be called the "X-factor".
5. The demonstration of convection mixing in sealed target cells with no moving parts.

Of the above mentioned points, only the first, the use of alkali-hybrid mixtures, was employed during GEN-I. By itself, however, this made it possible to maintain a target polarization of roughly 50% with 8 μA of beam on target, considerably better than the range of mid-thirty to low-forty percent polarizations that had been achieved previously. Prior to GEN-I, spin-exchange polarized targets generally used a single alkali metal, rubidium, in the spin-exchange process. When using rubidium, the efficiency with which angular momentum makes its way from circularly polarized photons to ^{3}He nuclei is only a few percent. Alkali-hybrid technology involves the use of a mixture of rubidium and potassium. Potassium, it turns out, is much more efficient at transferring its electronic polarization to ^{3}He nuclei through spin exchange. When alkali-hybrid mixtures are used, the efficiency with which angular momentum is transferred can be as high as 20–30%. This single advancement made it possible to achieve unprecedented target performance during GEN-I.

The second and third advancements listed above have resulted in improvements to target performance that are at least as significant as those that were achieved by employing alkali-hybrid technology. For the first time, we have begun making target cells that regularly (in the *majority* of those tested) achieve ^{3}He polarizations in excess of 70%. Two factors have contributed to this improvement. First, we have optimized the ratio of potassium to rubidium, a process that required more sophisticated target diagnostics. Secondly, we have begun using a new type of commercial line-narrowed high-power diode-laser arrays. Among other things, the new lasers make it possible to maintain alkali-vapor polarizations near 100% even at very high alkali number densities. The

polarized ^{3}He experiments that are currently running in Hall A are benefitting from these developments. The transversity experiment, for instance, is running with polarizations well in excess of 60% despite the fact that the experiment requires frequent flipping of the ^{3}He polarization direction, which causes significant loss of polarization.

The fourth and fifth advancements are of particular relevance to GEN-II. With the implementation of advancements 1–3, the rate at which we can polarize ^{3}He nuclei is sufficient to overwhelm rapid depolarization due to the electron beam, even at high beam currents of tens of microamps. As we will show below, however, the basic target-cell design that has been used at JLab in recent years has an intrinsic limitation. The ^{3}He is polarized in an upper "pumping chamber", whereas the electron beam is incident upon the polarized gas in a lower "target chamber". The connection between these two chambers has historically been accomplished using a single glass tube, referred to as the "transfer tube". The mixing of gas between these two chambers has been dominated by diffusion, and characterized by time constants on the order of 30–40 minutes. While these mixing times have been quite adequate in the past, we are now able to polarize the gas so quickly that a substantial polarization gradient exists between the pumping chamber and the target chamber. This polarization gradient would be unacceptably large at the currents at which we plan to run GEN-II. To solve this problem, we have developed a new technique in which convection, not diffusion, causes the mixing of the gas. This is the fifth advancement mentioned above. Finally, the fourth advancement (which chronologically came earlier), was the identification of a previously unrecognized relaxation rate. This discovery, made by Thad Walker's group at the University of Wisconsin, has made it possible for us to understand the behavior of our targets at a level of detail that was not previously possible. For the first time, we are able to make measurements in our lab that allow us to predict with considerable accuracy the behavior that we see under full operating conditions.

In summary, the high-luminosity GEN-II target is based almost entirely on ideas that have either been demonstrated previously in Hall A, or ideas that have subsequently been tested in our lab. The "Transversity" experiment currently running in Hall A already has benefitted from polarizations as high as roughly 70%. With a few additional features, The GEN-II target will be able to run with 60% polarization even with a beam current of 60 μA, and an increased target length of 60 cm instead of 40 cm. The key new features that will make it possible to go to high currents include a cell that utilizes convection to enable rapid mixing, a metal target chamber, and a larger pumping chamber that will provide a bigger reservoir of polarized gas. The target will use ten spectrally-narrowed high-power diode-laser arrays. We note that some polarized ^{3}He experiments at JLab have used as many as seven lasers in the past. In short, with the substantive advances that have occurred with polarized ^{3}He targets in recent years, the GEN-II target is actually not a very ambitious jump at all. Rather, we are planning to take advantage of improvements that already exist.

4.2.1 The principles behind the GEN-II target

The polarized ^{3}He target is based on the technique of spin-exchange optical pumping which can be viewed as a two step process. In the first step, an alkali-metal vapor (in our case containing a mixture of potassium (K) and rubidium (Rb)) is polarized by optical pumping using radiation from a laser. In the second step, the polarized alkali-metal atoms collide with the ^{3}He atoms, transferring

their spin to the ^{3}He nuclei through a hyperfine interaction. For the polarized ^{3}He targets that have been used at JLab both the alkali vapor and the ^{3}He are contained in sealed glass cells, an example of which is shown in Fig. 8.

Figure 8: Shown is one of the glass polarized ^{3}He target cells used during GEN-I (E02-013).

If the diffusion time between the pumping chamber and the target chamber is fast enough that it can be neglected, the time dependence of the ^{3}He polarization has a particularly simple form

$$P_{\mathrm{He}}(t) = P_{\mathrm{Alk}} \frac{\gamma_{se}}{\gamma_{se}(1+X)+\Gamma}\left(1-e^{-t(\gamma_{se}+\Gamma)}\right), \tag{16}$$

where P_{He} is the nuclear polarization of the ^{3}He, P_{Alk} is the polarization of the alkali-metal vapor, γ_{se} is the rate of spin-exchange rate between the ^{3}He and the Rb, and Γ is the spin-relaxation rate of the ^{3}He nuclei due to all other processes. The factor $(1+X)$ accounts for what is now a well-established additional relaxation mechanism whose presence has been empirically established but whose origin is unknown [58]. The factor $(1+X)$ has the form given because the additional relaxation mechanism has been seen to be roughly proportional to the alkali-metal number density. We note that the factor "X" can be measured for any particular cell, and is one of the quantities that we have begun to measure for the various target cells that we produce.

The spin exchange rate can be written

$$\gamma_{se} = f_{pc}(k_{se}^{\mathrm{K}}[\mathrm{K}] + k_{se}^{\mathrm{Rb}}[\mathrm{Rb}]), \tag{17}$$

where f_{pc} is the fraction of ^{3}He atoms that are located within the pumping chamber, $k_{se}^{\mathrm{K}}(k_{se}^{\mathrm{Rb}})$ is the constant characterizing spin exchange between ^{3}He and K(Rb), and [K]([Rb]) is the number density of K(Rb) atoms within the pumping chamber. It can be seen that in order to achieve high polarizations, we must have the relaxation rate $\Gamma << \gamma_{se}$. In principal, if the alkali-metal number density can be made arbitrarily high, the ^{3}He polarization can approach the limiting value of

$P_{\rm Alk}/(1+X)$. In the past, the highest alkali-metal number density that could be maintained at something approaching 100% was strongly limited by the available laser power. By using alkali-hybrid mixtures and line-narrowed lasers, however, it is now possible to use very high alkali number densities.

The spin relaxation rate Γ contains several contributions and can be written

$$\Gamma = \Gamma_{wall} + \Gamma_{bulk} + \Gamma_{beam}, \tag{18}$$

where Γ_{wall} is spin relaxation due to collisions between the ^{3}He atoms and the container walls, Γ_{bulk} is spin relaxation due to ^{3}He-^{3}He collisions, and Γ_{beam} is spin relaxation due to the electron beam. For our target cells, the time constant associated with spin relaxation due to wall collisions and bulk effects, $(\Gamma_{wall}+\Gamma_{bulk})^{-1}$, is usually in the range of 20–40 hours. The beam depolarization rate has been studied both theoretically [59] and experimentally [60] and is given by

$$\Gamma_{beam} = (76,292\,{\rm cm}^2/{\rm g})\,\rho_{\rm He}\,L_{tc}\,J_{beam}/N_{He}, \tag{19}$$

where $\rho_{\rm He}$ is the mass density of ^{3}He in the target chamber, L_{tc} is the length of the target chamber, J_{beam} is the beam current in particles per unit time, and N_{He} is the total number of ^{3}He atoms in the target. The time constant associated with with beam depolarization, $(\Gamma_{beam})^{-1}$ was on the order of 100 hours during GEN-I. For GEN-II, for our proposed target configuration, it will be about 20 hours at 60 μA. The GEN-II target incorporates two features that suppress depolarization due to the electron beam. First, convection-based mixing will be used to eliminate the polarization gradient between the pumping chamber and the target chamber. Secondly, the pumping chamber will be substantially bigger, providing a large reservoir of polarized gas. The GEN-II target is based on a design in which 6.8 STP liters of gas are polarized. In contrast, the GEN-I target was based on a design in which 3 STP liters of gas were polarized.

4.2.2 The GEN-I polarized ^{3}He target and subsequent studies.

The figure of merit for the polarized ^{3}He target during GEN-I was the highest that had ever been achieved by a polarized ^{3}He target during an electron scattering experiment. The figure of merit for the current "Transversity" experiment is even higher still, but as only on-line data are available at this time (the experiment is still running at the time of this writing), we will restrict our comments on the Transversity targets to measurements made in our lab at UVa. The polarization achieved as a function of time for the GEN-I cell "Edna", used for the majority of our data taking, is shown in Fig. 9. The polarization of the target was near or even above the 50% level for more than 50 days of running with beam currents that were typically about 8 μA. The polarization was well above the 40% level assumed in the original GEN-I proposal. Furthermore, while we ran at 8 μA, there is little question that the target would have performed well at 12 μA, the original design current. There were several factors that contributed to the high performance we observed, but central among them was the use of alkali-hybrid technology, the first time this approach was used in an electron scattering experiment.

The physical configuration of the GEN-I target is illustrated in Fig. 10. The magnetic holding field for the polarized ^{3}He was provided by a soft iron box that was magnetically excited using several sets of coils. This technique was economical in the use of space and was effective in reducing magnetic field gradients that were held below 10 mG/cm. The glass target cells were

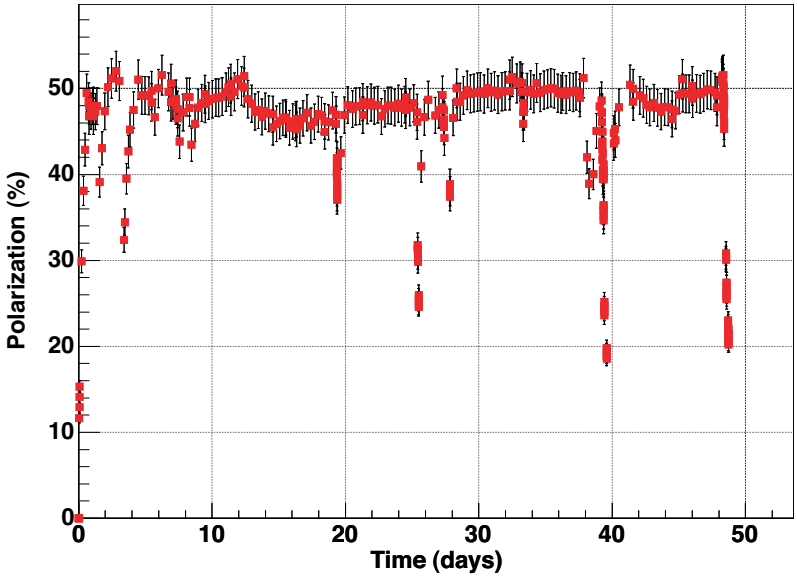

Figure 9: The polarization (in the target chamber) of Edna, the target cell with which the majority of the data were obtained during GEN-I (E02-013). The figure of merit of Edna is unprecedented in the history of the use of polarized ^{3}He during an electron scattering experiment.

mounted on a movable target ladder (shown at right in the figure) that could be moved in and out of the beam as needed while continuously illuminating the target cell with laser light. The laser light was provided by several high-power diode-laser arrays that were outside of Hall A, and the light was transported to the target using optical fibers. While the exact geometry of the target for GEN-II has yet to be worked out in detail, the experience gained during GEN-I make it clear that we will have no difficulty operating in the high fringe fields of the BigBite (electron arm) and BigBen (neutron arm sweeping magnet) magnets. This is particularly true because during GEN-II, as will be described more in the next section, we plan to relax the requirements for magnetic-field homogeneity for the target chamber. The GEN-II target will also use a fiber-optic-based optics system that builds on the system developed for GEN-I and currently in use for the Transversity experiment.

Despite the excellent performance achieved during GEN-I, there was an aspect of the GEN-I target-cell design that limited its performance. As discussed earlier, the pumping chamber, in which spin exchange takes place, and the target chamber, through which the electron beam travels, were connected by a single glass tube referred to as the “transfer tube”. Mixing between the two chambers occurs largely because of diffusion, and was characterized by a time constant of around 30–40 minutes. Historically the length of this time constant did not significantly limit the target’s performance, as the time constants characterizing polarization were much longer, around 20 hours. During GEN-I, however, because of the very efficient use of laser light, it was possible to run the target in a mode in which the time constants characterizing the buildup of polarization were on the order of six hours. When the electron beam was incident on the target and thus causing depolarization, diffusion limited the rate at which the polarization in the target chamber could be replenished by the pumping chamber. This caused a significant polarization gradient between the

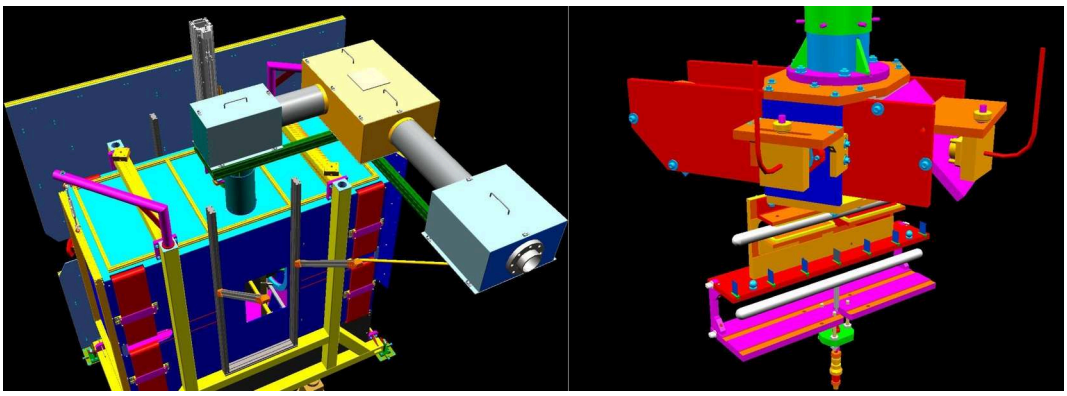

Figure 10: Shown are engineering renderings of the polarized ^{3}He target used during GEN-I (E02-013). At left is an overview of the entire target, the largest feature being the soft iron box that, together with several coils used to magnetically energize the box, provided the magnetic holding field. Also visible on the left is the optics system (contained in three boxes mounted on top of the target) that provided circularly polarized laser light to the target. On the right is a close-up of the target ladder.

pumping chamber and the target chamber. Fig. 9 shows the polarization as measured in the target chamber to be in the range of 47–52%. The polarization in the pumping chamber, however, was typically about 4.5% higher, or 51.5–56.5%.

The phenomenon of polarization gradients between the pumping chamber and the target chamber is something that we have now studied extensively at UVa. Even in the absence of the passage of an electron beam through the target chamber, the polarization gradient can be quite significant. An example of the effect is illustrated in Fig. 11, in which the polarization of both the pumping chamber (upper trace) and target chamber (lower trace) are shown as a function of time. In this particular test the cell was being run quite "hot", that is, the time constant characterizing the spin-exchange time constant in the pumping chamber was around 4–5 hours. For this particular study, the gradient between the pumping chamber and the target chamber was around 7%. Polarization gradients have important implications if one is interested in running significantly higher beam currents. No matter how quickly gas can be polarized in the pumping chamber, the polarization in the target chamber will be limited if the gas does not move sufficiently quickly between the two chambers. We have solved this problem using a new approach based on convection that will be discussed more in the next section.

The study of polarization gradients illustrated in Fig. 11 is but one example of an extensive set of studies that have been performed at UVa in the time period following GEN-I and in preparation for the current set of polarized ^{3}He experiments that are running in Hall A. Perhaps the most dramatic result of these studies was the establishment of polarizations that were consistently 70% or better. As mentioned earlier, there were two closely interacting factors that contributed to the big increase in target performance. One was the careful optimization of the hybrid technology using a new set of diagnostics that made it possible to measure not just the nuclear polarization of the ^{3}He, but also the polarization and number densities of the Rb and K vapor. The other was the opportunity to use, for the first time, high-power diode-laser arrays with spectral widths of around 150 GHz, much narrower than than the roughly 1000 GHz spectral width of the lasers we had been using

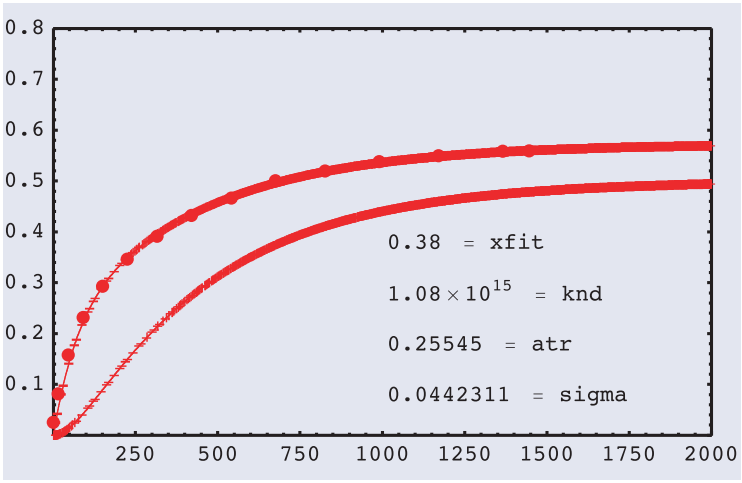

Figure 11: Data on the polarization of the target cell Simone as a function of time together with fits from a model that incorporates the effects of polarization gradients due to the limited rate of diffusion between the two chambers of the target cell. The upper trace shows the polarization in the pumping chamber and the lower trace shows the polarization in the target chamber. This figure illustrates the necessity of using convection instead of diffusion for targets that will be used in high-current electron beams.

previously. With our optimized target cells, the new lasers, and our improved diagnostics guiding us, we saw huge improvement in target performance. Perhaps best of all, we have established the most detailed understanding of the physics occurring within our targets that we have ever had. This last point is critical, because it makes it straightforward to design an appropriate target for GEN-II.

4.2.3 The GEN-II High-Luminosity Target Cell

The high-luminosity GEN-II target cell represents a natural evolution of the GEN-I target cell, but incorporates two critical new features. First, instead of relying on diffusion to move gas between the pumping chamber and the target chamber, the new GEN-II cells will utilize convection. Second, the GEN-II target cells will be constructed out of both glass and metal. Specifically, the pumping chamber, in which the optical pumping and spin exchange take place, will be constructed out of glass, and the target chamber, through which the electron passes, will be constructed out of metal. Taken together, these two new features will make it possible to run the new target at very high currents. A rough conceptual design of the GEN-II target cell is shown in Fig. 12.

Ever since adopting alkali-hybrid technology, the rate at which ^{3}He nuclei are being polarized in our targets is sufficient to compensate for a considerable amount of beam depolarization. As discussed in the last section, however, the rate at which polarized gas in the pumping chamber moves into the target chamber is limited by diffusion. Up to this point, all polarized ^{3}He cells used at JLab have had a geometry similar to that of the cell depicted in Fig. 8 in which a single “transfer tube” connects the pumping chamber to the target chamber. In the GEN-II cell geometry, however, two transfer tubes are used. With this geometry, one of the transfer tubes can be heated in order to drive convection, and the gas in the two chambers can be mixed as quickly as is desired. In fact, once control is established over the mixing times, the pumping chamber and the target chamber can

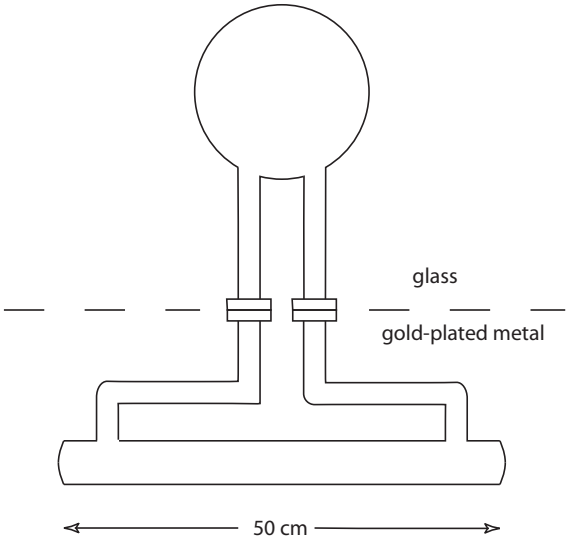

Figure 12: A conceptual design for the GEN-II target cell. Two transfers tubes connect the pumping chamber to the target chamber to make it possible to drive convection between the two cells. Also, the upper portion of the cell is made of glass, whereas the lower portion is made of metal, probably gold plated aluminum. The two sections are connected to one another using a flange system that captures a gasket made of either indium or gold.

be physically separated by substantial distances, and even the magnetic fields of the two regions can be controlled independently.

The second feature that distinguishes the GEN-II cell from its predecessors is the use of a metallic target chamber. Our experience suggests that after something like 3–6 weeks of beam in the range of $5-8\,\mu$A, our all-glass target cells tend to explode. There is strong evidence that these catastrophic failures occur because of radiation damage, a problem that is certain to get much worse with substantially higher beam current. With a metal target chamber, however, the portion of the target that sees high radiation becomes quite robust. While we have not previously used metal in our ^{3}He targets, it is important to point out that we have considerable experience using metal in the ^{3}He polarizers that our group has constructed for medical imaging. In this work, we have found aluminum to be particularly benign from the perspective of spin relaxation. In our medical applications, however, the ^{3}He nuclei spend less time in contact with metal then will be the case in the GEN-II target. We can glean some insight, however, from data taken by Ernst Otten's group at Mainz who measured a spin relaxation rate of $1/6$ hours on aluminum, and $1/20$, hours on gold [61]. Many of our target cells have intrinsic spin-relaxation times on the order of $1/25$, hours, only marginally better than the wall relaxation induced by gold. Furthermore, in the GEN-II target, the ^{3}He gas will be continually circulating because of the convection and will only reside in the metal target chamber something like 20% of the time. Our group has had quite favorable experience working with gold coating in optical pumping applications. Thus, based on both our own past experience as well as that of the group at Mainz, we are planning to use a gold-coated aluminum target chamber. For the glass-to-metal seal, we will employ a large glass flange coupled to a large metal flange that collectively will sandwich an o-ring. Our first choice would be an o-ring made of either gold or indium. We note, however, that the cells we use for medical

imaging all contain a polymer-based o-ring, and that is an acceptable solution. In summary, the challenges associated with the GEN-II target cell are not unlike the issues that we have already successfully faced in the context of medical imaging. Some development work will be required, but the important underlying materials issues, such as the spin-relaxation properties of the needed materials, have already been addressed.

4.2.4 Convection Tests in a Prototype GEN-II Target Cell

As has already been emphasized, the success of the GEN-II target relies critically on our ability to circulate the polarized gas between the pumping chamber and the target chamber using convection. Indeed, this is the enabling technology for the GEN-II target, because it allows us to use a sealed cell with no moving parts. We thus felt that demonstrating our ability to drive convection would remove important uncertainties regarding the GEN-II target design. With this in mind, we constructed an all-glass sealed cell that approximates the basic geometry of the GEN-II target. The dimensions were chosen not to correspond to what we would ultimately like to build, but rather so that the test cell could be fabricated and tested using our existing apparatus. The resulting cell is shown in Fig. 13.

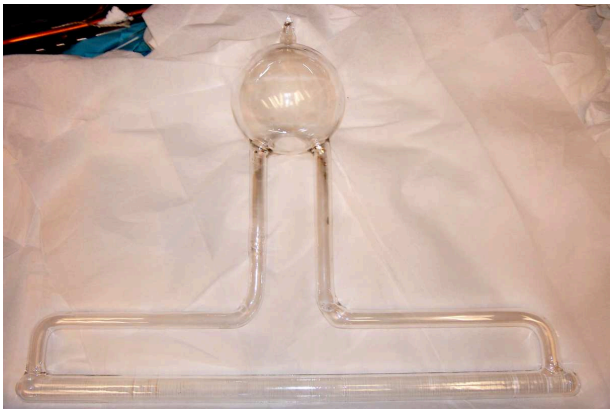

Figure 13: The first prototype "convection-driven target cell. Made entirely out of glass, this cell approximates the geometry of the proposed GEN-II target-cell geometry and is being used to prove the concept of mixing the gases of the pumping chamber and target chamber using convection.

To drive convection, a small hot-air driven heater was attached to the right-hand transfer tube leading out of the pumping chamber. To detect and characterize the convection, a small slug of gas was "tagged" by depolarizing it using a short pulse of resonant RF delivered by a small "zapper coil" that was wrapped around the left-hand transfer tube. The movement of the tagged slug of gas was tracked using a set of four "pick-up coils" that were spaced equally along the length of the target chamber. A photograph of the instrumented prototype cell is shown in Fig. 14.

Representative data from our tests are shown in Fig. 15. At $t = 0$, a pulse of RF was delivered by the zapper coil, creating a depolarized slug of gas. The polarization of the gas passing through the four pick-up coils was monitored by making an NMR measurements every 5 seconds using the technique of adiabatic past passage. Each of the four coils clearly shows the passage of the depolarized gas as evidenced by the time dependence of the measured polarization. The first transient

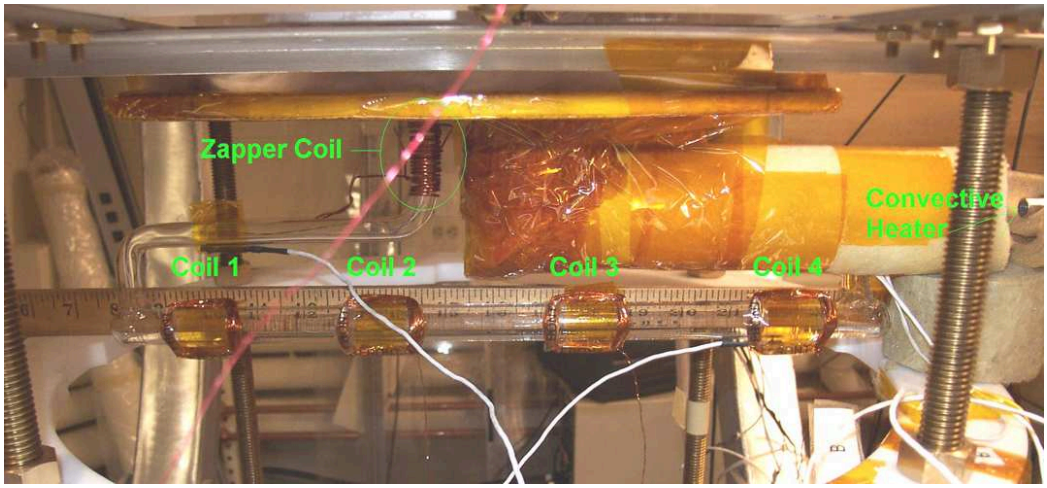

Figure 14: The prototype convection-driven target cell is shown instrumented for tests. As described in the text, a "zapper coil" is used to tag a slug of gas, and four pick-up coils monitor the movement of the tagged slug of gas through the target chamber. The speed of the convection is controlled using the "convection heater".

of reduced polarization appears in coil #1, the most upstream coil. Transients subsequently appear in each of coils #2–#4. It is interesting to note that the transient is relatively narrow as observed by coil #1, but broadens when observed by each successive coil. This is because diffusion is causing the slug of depolarization to spread out. Finally, we note that the data are of sufficient quality that we can compute the speed of the gas, which in this case, was around 20 cm/min.

We were able to control the speed with which the gas moved by adjusting the temperature of the heater attached to the left-hand transfer tube. The data shown in Fig. 15 were taken at 50°C. In Fig. 16, we show the results of measurements corresponding to setting our heater at temperatures between roughly 31°C and 67°C. Gas speeds in excess of 30 cm/min were observed. At such speeds, the gas in the target chamber will be replaced with new gas every two minutes, roughly 20 times faster than was the case during GEN-I. The implications of using convection-driven polarized ^{3}He targets are quite profound. First, we are no longer limited in the speed with which we can replenish gas that has been depolarized by the electron beam. In addition, however, we are for the first time in a position to physically separate the region in which the ^{3}He is polarized from the region in which the ^{3}He serves as a target. Among other things, this provides considerable flexibility in the manner in which we generate magnetic holding fields, a matter that we will return to shortly.

4.2.5 Choosing Design Parameters for the GEN-II High-Luminosity Target

Using nothing more than the formalism presented earlier in the target section, it is straightforward to compute the expected performance for a given target design. Many of the inputs are quite unambiguous, such as target cell geometry, ^{3}He density, and the expected depolarization due to interaction with the electron beam. Some of the inputs are specific to a given cell, such as the intrinsic spin-relaxation rate associated with a particular target cell, and the value of the so-called $X-$factor that characterizes the now well-established but poorly-understood relaxation mechanism

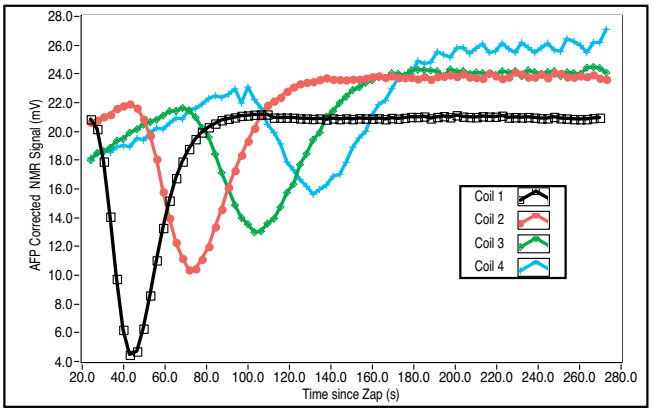

Figure 15: Shown are NMR signals from the four equally-spaced pick-up coils that were mounted on the target chamber as a function of time where $t = 0$ corresponds to the creation of a depolarized slug of gas. Coil #1 was the most upstream coil, given the expected direction of flow. Transients corresponding to the passing of the depolarized gas are clearly visible (in the expected order) for each of the four coils.

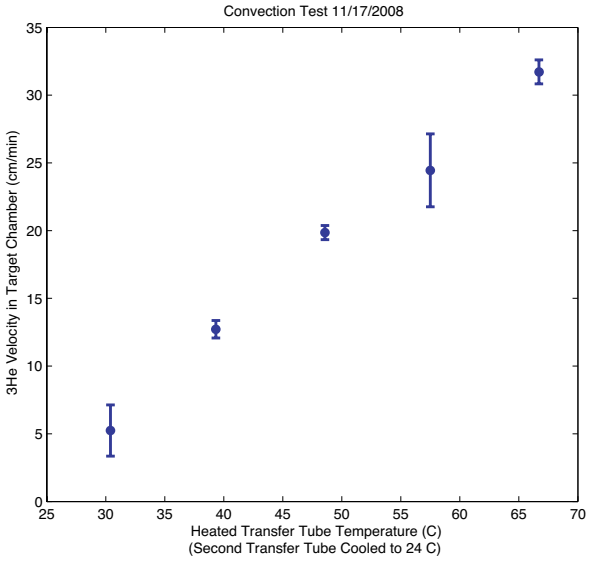

Figure 16: The measured speed of the gas moving through the target chamber is plotted as a function of the temperature of the "convection heater". At 30 cm/s, the gas in the target chamber is replaced every 2 minutes, roughly 20 times faster than was the case during GEN-I.

that scales with alkali density. While these values are cell specific, we have measured them on a sufficient number of cells that we know with confidence what is achievable. Finally there is laser power, along with its implications for the maximum number density of alkali-metal atoms that can be maintained at very high polarization. In principle, the literature contains sufficient information to compute the required laser power for a particular set of operating conditions. We believe, however, that a more conservative approach is to formulate an estimate based on scaling.

We present in Fig. 17 (in the right-hand plot) the predicted performance for the GEN-II target. With a beam current of $60\,\mu$A, a target-chamber length of 60 cm, an intrinsic cell-specific spin-relaxation rate of $1/25$ hrs, and an "$X-$"factor of 0.15, we predict a target polarization of 62%. For comparison, we have also calculated the expected polarization in a cell similar to what is currently being used in the "Transversity" experiment, but at $60\,\mu$A. Assuming diffusion to be infinitely fast, the expected polarization would be around 45%. The difference is that the GEN-II target incorporates a large reservoir of polarized gas in the pumping chamber, ensuring that the *fraction* of ^{3}He nuclei being depolarized is smaller than would otherwise be the case. I note also that we have assumed in this comparison that the target chamber length of the Transversity-type cell was 60 cm (not the actual length of 40 cm) so that the absolute rate of beam depolarization would be the same for either target. Finally, when we calculate (not shown) the polarization that one would expect during the existing Transversity experiment, we get roughly 70%, just as observed, at least when the target polarization is not being rapidly flipped back and forth.

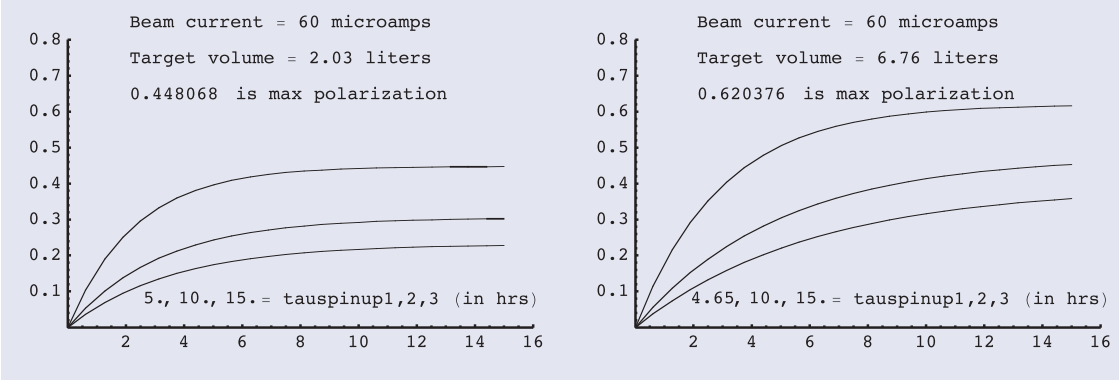

Figure 17: Shown are calculated "spin-up" curves for cells similar to those being used in the Transversity experiment (at left) and a cell with characteristics such as are planned for GEN-II (at right). For the GEN-II design, a polarization in excess of 60% is achieved at a beam current of $60\,\mu$A.

4.2.6 The Physical Configuration of the GEN-II Target

Having established the feasibility of running the GEN-II target at high luminosity, we include here a few comments on other aspects of the design.

First, the target chamber of the cell, that is, the metallic portion of the sealed polarized ^{3}He target cell, will sit in a vacuum. While this has not been the practice at JLab, we note that the polarized ^{3}He target cells used in both E-142 and E-154 (two experiments at SLAC that studied the spin structure of the neutron) sat in vacuum. At SLAC, however, this was quite challenging because

it meant that even the oven that provides heat to the pumping chamber needed to sit in vacuum. The GEN-II target, however, will have a metal target chamber. It will thus be straightforward to have the target chamber sit in vacuum while the pumping chamber, along with optics, NMR components, etc., sit outside the vacuum.

Next, we comment on the magnetic holding fields. For GEN-II, we will only perform NMR measurements on the pumping chamber, not the target chamber. Historically, the magnetic field homogeneity requirements for the JLab polarized ^{3}He targets have been driven by the need to minimize polarization losses during NMR measurements. This will still be true for the pumping chamber, but not for the target chamber. Assuming that we use a holding field of roughly 20 Gauss, the homogeneity requirement for the pumping chamber will be roughly 5–10 mG/cm. For the target chamber, however, the requirement will be roughly 200 mG/cm, a factor of 20–40 less demanding. Furthermore, we plan to control the magnetic field at the target chamber *independently* from the magnetic field in the pumping chamber. The two fields can even point in arbitrarily different directions. It will take roughly 2–3 minutes for gas to travel from the pumping chamber, down through the target chamber, and back into the pumping chamber. This is more than enough time for the spins to adiabatically follow the magnetic field through an arbitrary change in direction with negligible loss of polarization. One of us (Cates) used essentially this technique in an experiment at Los Alamos in which polarized muonic ^{3}He was produced by stopping muons in polarized ^{3}He gas [62]. The holding field for the ^{3}He was adiabatically rotated once every two minutes by 180°, and no measurable loss of polarization was detected. Finally, since the magnetic field surrounding the target cell can point in an arbitrary direction, it can also be flipped at will. If done sufficiently smoothly, we believe it should be trivial to flip the magnetic field of the target chamber in ten seconds or less. We note the limitation on the flipping speed (without polarization losses) comes not from quantum mechanics, but from the smoothness with which the flip is accomplished. For the SIDIS experiment, we plan to flip the target direction once every two minutes, losing less than 10% of the data-taking time in the process.

4.3 The BigBite Spectrometer

Scattered electrons will be detected in the BigBite spectrometer (Fig. 18). BigBite is a non-focusing large momentum and angular acceptance spectrometer that was originally designed and built for use at the internal target facility of the AmPS ring at NIKHEF [63, 64]. The spectrometer consists of a single dipole magnet (with magnetic field approximately 1.2 T) and a detection system. The current electron detector package includes three sets of multi-wire drift chambers, a gas Cerenkov detector, a segmented lead glass calorimeter in two parts knows was the preshower and shower, and a plastic scintillator plane between the shower. Summed amplitudes over the preshower and shower form the trigger.

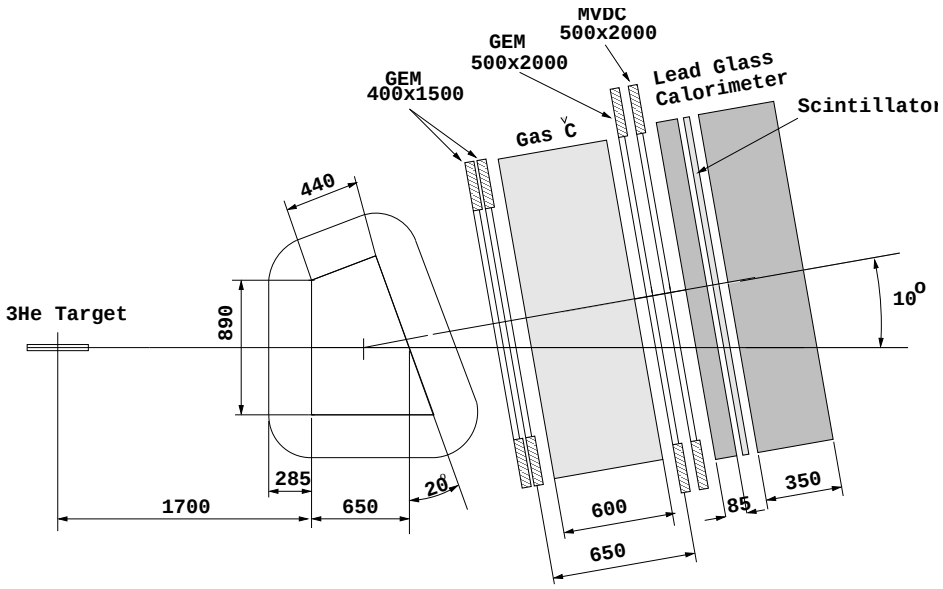

Figure 18: The BigBite spectrometer with proposed detector stack.

4.3.1 GEM Chambers

To cope with the high rates for this experiment, the drift chambers will be replaced with gas electron multiplier (GEM) detectors [65]. These detectors have proven to be capable of operating under luminosities of 25 kHz/mm^2 for the COMPASS experiment at CERN [66] and the spatial resolution of each of these chambers is anticipated to be about 70 μm. For two sets of two GEM chambers separated by a distance z_{GEM} and including multiple scattering effects, the angular resolution of the drift chambers can be approximated by

$$(\delta\theta)^2 = \frac{\sigma_x^2}{z_{\mathrm{GEM}}^2} + \left(\frac{13.6\ \mathrm{MeV}}{\beta c p} \sqrt{x/X_0}\,[1 + 0.038 \ln(x/X_0)] \right)^2 \tag{20}$$

where βc is the velocity of the electron, p is the momentum of the electron, and x/X_0 is the thickness of the scattering material in radiation lengths.

For small deflection angles from a dipole magnet, the deflection angle, θ, and the momentum, p, are related by the equation

$$p = \frac{e \int B_{\perp} \cdot dl}{\theta}, \tag{21}$$

where $\int B_{\perp} \cdot dl$ is the field integral for the path of the electron. For electrons of momentum $3 \sim 4$ GeV and a field integral of 1.0 T · m, this would yield a typical momentum resolution of $\delta p/p \approx 0.5\%$.

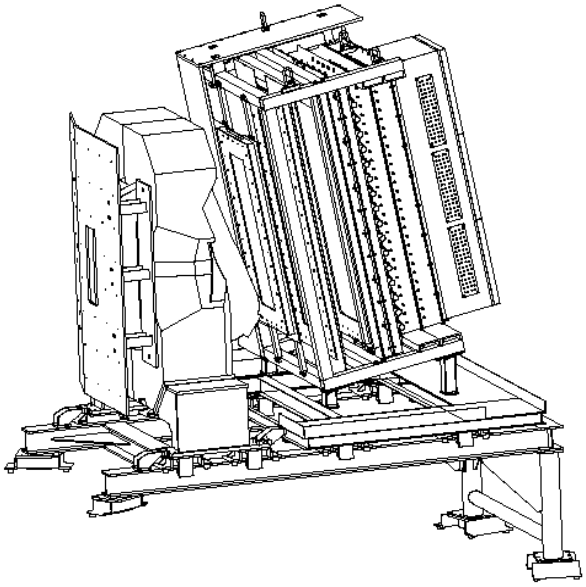

Figure 19: The BigBite spectrometer with the current electron detector stack.

In order for us to accurately determine the scattered electron's angular coordinates, momentum, and the position of the scattering vertex along the target, the optics of BigBite need to be studied. Data from a multi-foil carbon target and a removable lead sieve located at the front face of the magnet provide an accurate method to calibrate the angular coordinates before magnetic deflection and a beamline scattering vertex position. Data from elastic coincidence ep scattering from a H_2 target will provide data to calibrate the electron momentum and will be performed for each beam energy setting. As the kinematics for quasielastic and elastic scattering are similar, this provides the most efficient and reliable method for calibration. With the sieve plate in place, it also eliminates the need for $B = 0$ field data, which was proven difficult to extract due to prohibitively high rates of otherwise deflected low energy particles.

4.3.2 Simulation of BigBite

Two packages of programs for the simulation of the BigBite spectrometer characteristics were developed independently by V. Nelyubin [67] and S. Riordan. For this experiment, the momentum of the scattered electrons will be approximately 3.5 GeV/c for the $Q^2 = 10$ GeV^2 point, leading to an expected momentum resolution of δp/p of about 0.5%. The expected position resolution on

target along the beam is σ= 4 mm, and the expected angular resolution in both scattering planes is better than σ=0.3 mrad.

Additional MC studies were done to evaluate the parameters of the proposed experiment. The range of Q^2 accepted by the electron arm is shown in Fig. 20. The solid angle of the electron arm for different positions along the target is shown in Fig. 21. The average solid angle for our maximum electron energy is about 44 msr.

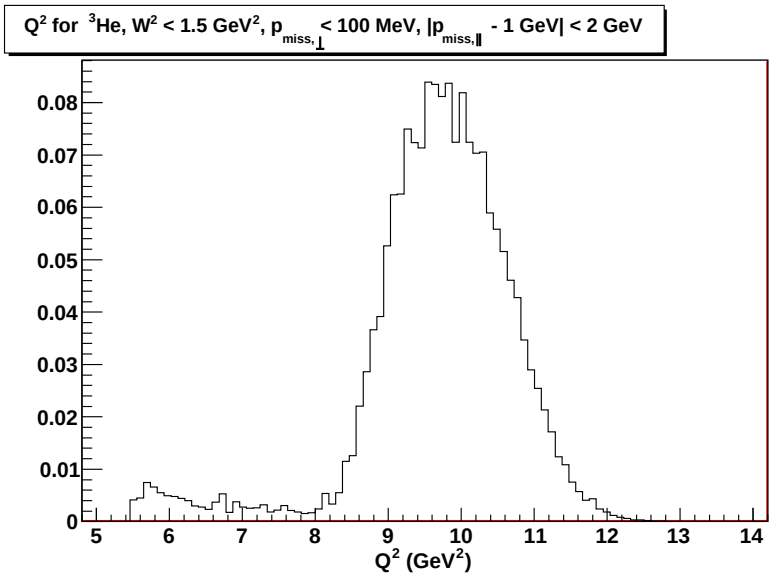

Figure 20: The momentum transfer range accepted in the BigBite spectrometer for the $Q^2 = 10$ GeV^2 point.

4.3.3 Background Rate in BigBite

Several MC simulations [68] and real data sets [36] were used for the calculation of the rate on the BigBite detectors. Charged particles with momenta below 300 MeV/c will be deflected entirely out of the acceptance by the BigBite dipole. The majority of charged background particles with momentum above 300 MeV/c are π^-, and for pions near quasielastic electron momentum, are about a factor of 3 higher in rate than electrons (Sec. 6.2). With an overall pion rejection factor of 10000:1, this number can be reduced to a negligible amount.

The total trigger rate on the shower/preshower with a threshold of 1.7 GeV is expected to be about 2 kHz from a simulation based on pion production rates from a parameterization done by Wiser [69], Fig. 22. This simulation when compared to the previous G_E^n experiment predicted rates higher by a factor of 5, so this produces an upper limit on expected rates. Furthermore, adding the Cerenkov into the trigger configuration to explicitly reject pions and photons will be possible if necessary.

A majority of hits in the GEM chambers will be produced by photons. To investigate the photon detection probability a separate GEANT-4 code was used. The GEM geometry and materials were chosen to be the same as in the COMPASS chambers. The probability to produce a secondary electron in the drift gap of the chamber as a function of the energy of the initial soft photon is

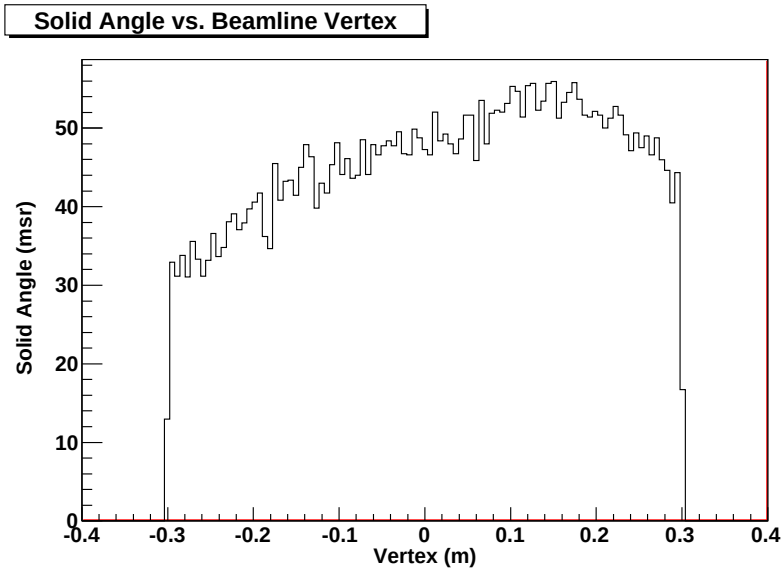

Figure 21: The MC simulation of the BigBite solid angle versus the position on target along the beam direction.

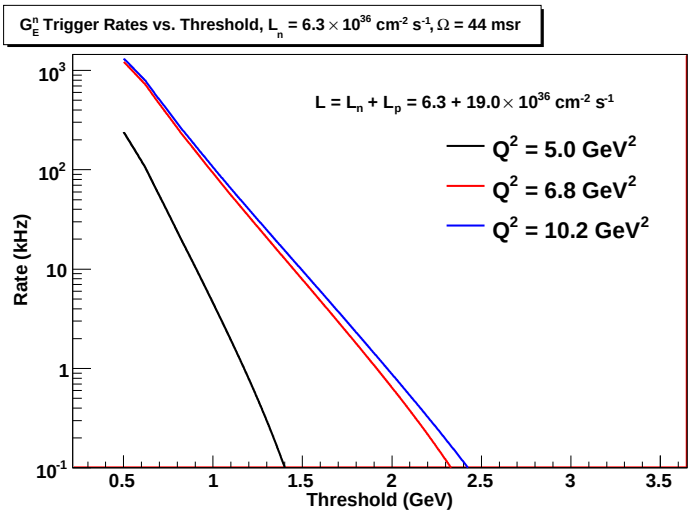

Figure 22: Anticipated trigger rates for each setting.

shown in Fig. 23. It is about 10^{-3} at 100 keV and increases up to 4×10^{-3} at 1 MeV. Above 1 MeV the photon efficiency (Fig. 24) increases but doesnt exceed 1%. In the same figures, bottom panels, the probability for correlated hits in two or more chambers is shown. This happens when one photon produces secondary electrons in several chambers. One can see that such a probability is negligible for photon energies below 1 MeV, and the hit rates on the chambers are dominated by uncorrelated random hits.

Using data from the Transversity experiment, E06-010, which placed BigBite at 30° at 1.5 m with a beam current of 12 μA, the rate per 140 cm $\times$ 35 cm chamber was 41 MHz. At our beam energies, beam current, active area, target length, and BigBite distance, we expect an increase in rate by about a factor of 13. Estimating the BigBite drift chamber photon efficiency to be at most a factor of 5 smaller than the GEM chambers, we anticipate an overall increase in the observed rate in the drift chambers to be a factor of 65, or a rate of 4.5 kHz$/$mm^2. This is below rates in which these have been demonstrated to operate.

Using information from the shower and scintillator, the area in the GEM chambers to search for tracks can be restricted by a factor of 10, leading to approximately 26 false hits in a 100 ns time window per plane. Current transversity tracking code operates with a time window larger by a factor of three and without using shower information, presenting an overall background rate the tracking must contend with higher by only a factor of two. This should present no problem for current BigBite tracking software.

Using rates of charged particles above 300 MeV, less than 20% of events are anticipated to have multiple tracks in the same region as the triggering track. The *x* and *y* components of these tracks can be separated using the fixed *z* plane positions given by the shower and scintillator plane.

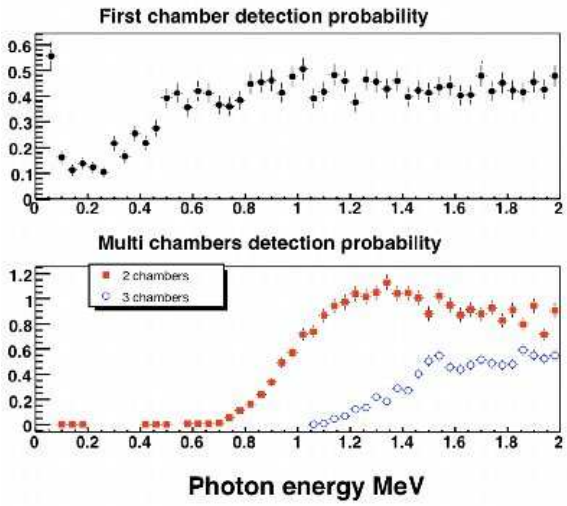

Figure 23: Top: Efficiency of registration in a single chamber of a soft photon as function of its energy. Bottom: probability for correlated hits in two or three chambers caused by a single soft photon as function of its energy. Scales are percent.

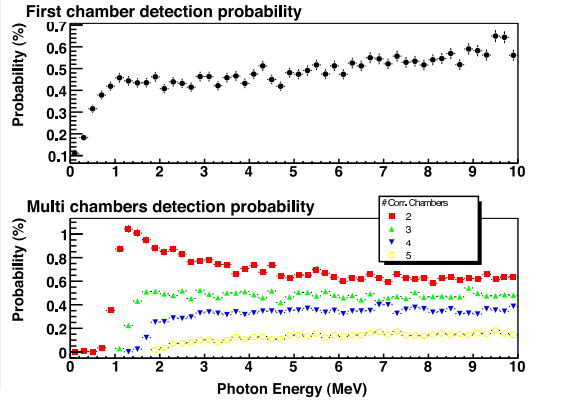

Figure 24: Same as Fig. 23, but in the 1-10 MeV region.

4.3.4 Shower/Preshower

The electromagnetic calorimeter configuration consists of two planes of lead glass blocks which which we call the preshower and shower. The preshower, located about 80 cm behind the first GEM chamber, consists of a 2×27 plane of 37 cm $\times$ 8.5 cm blocks. The shower, about 1 m behind the first GEM chamber, consists of an 7×27 array of 8.5 cm $\times$ 8.5 cm blocks. Sums over these blocks form the physics event trigger for the experiment.

The preshower signal can be used to provide an additional method of pion rejection. By selecting low preshower signals, a pion rejection factor of 1:50 can be achieved through optimization. Despite higher particle rates, pion rejection performance is anticipated to be similar to that achieved for Transversity, E06-010. By measuring the pedestal widths and resolution for E06-010 and scaling to this proposal's conditions, overall relative energy resolution for the detector is expected to become worse by a factor of 1.6, to about $\sigma_{\delta E/E} = 25\%$.

4.3.5 Scintillator

The BigBite scintillator plane will be upgraded from the current electron detector package to a configuration of 80 paddles in a plane, each with dimensions 1 in. $\times$ 1 in. $\times$ 60 cm. For the transversity experiment, where BigBite is at 30° using a shorter 40 cm ^{3}He target, and 12 μA beam, the rate for the scintillator plane was approximately 3.6 MHz. Using this data to provide upper limits on the rates seen for our experiment, scaling to current, a longer target, and bar active area, we anticipate a rate of 270 kHz per bar. This plane will primarily be used to provide a signal for nucleon time of flight reconstruction. A time resolution of 200 ps is anticipated.

4.3.6 Gas Cerenkov

The BigBite gas Cerenkov, consists of a tank with a maximum depth of 60 cm, with 20 spherical focusing mirrors in a 10×2 arrangement. Each primary mirror reflects onto a secondary mirror and in turn focuses light into a 5 in. PMT with a conical mirror to increase collection efficiency. Current commissioning has used C_4F_{10} as a radiator, however, with $n - 1 = 1.5 \times 10^{-3}$, the π

threshold is only about 2.5 GeV. For 12 GeV running, to provide a pion threshold of 3.5 GeV, a combination of about 50% CO_2, 50% Freon-12 will be used.

For our conditions, the rate of electrons will be about 30 kHz, which in a 100 ns gate will lead to a 0.3% chance of a pion being misidentified by an accidental electron. Using standard calculations, for a charged pion near threshold, there is a 0.1% chance of producing a δ electron above threshold. Combined, a pion rejection factor from the Cerenkov will be about 1:250, near specifications. Combined with a rejection factor of 1:50 for the preshower provides a 10^4 overall rejection.

4.4 Neutron Detector

The original design of the neutron detector for this experiment is based on many considerations, including detector acceptance, efficiency, and background suppression. For this experiment we propose using a very similar setup to that which was used in E02-013. There are several considerations which are specific to the conditions of the proposed experiment:

- The large kinetic energy of the neutron leads to the possibility of using high TDC thresholds and for off–line analysis.
- The relatively low luminosity for the polarized ^{3}He target and the presence of the BigBen magnet simplifies the background situation.
- The high velocity of the neutrons demands the largest possible distance from the target.

4.4.1 Structure of the Neutron Detector

This experiment is focused on large momentum transfer, where the recoiling neutrons have kinetic energies of 3.5 GeV, 4.4 GeV, and 6.3 GeV. Such large energies allow a high detection efficiency for neutrons, and at the same time they allow us to apply relatively high thresholds to suppress background from low energy particles. The previous detector layout is presented in Fig. 25, similar to what will be used. The overall dimensions of the neutron arm are $4.2 \times 2.0 \times 6.2$ m^3. The

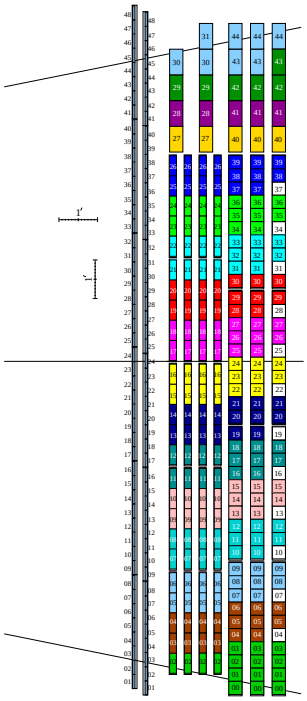

Figure 25: Side view of the neutron detector in E02-013. The irregular bars at the top will be replaced with bars similar to the others in the plane.

detector will have seven layers, consisting of 30 bars of dimensions $15 \times 5 \times 180$ cm^3 in the first three planes. In the fourth through seventh layers have 40 counters. These counters have dimensions $10 \times 10 \times 180$ cm^3. Each neutron bar is equipped with two photomultipliers, one on each end.

In front of every layer there is a 1.27 cm iron converter to increase the probability of a neutron interaction in the detector. The front of the detector will be covered by a segmented veto detector protected by a 1.27 cm thick iron plate and a 5.04 cm thick lead plate. Between the veto counters and the front layer of the neutron bars, there will be a 1.27 cm thick iron plate and a 5.04 cm thick lead plate from low energy particles.

4.4.2 Parameters of the Neutron Detector

The solid angle of the neutron detector is approximately 40 msr at a distance of 17 m from the target. The aspect ratio is 1:2.5. With such a geometry, the acceptance of the neutron detector nearly matches the acceptance of the BigBite spectrometer.

The time resolution is expected to be $\sigma_t = 0.3$ ns and was previously achieved in E02-013. At a distance of 17 m, the 0.3 ns time resolution leads to a neutron momentum resolution of $\sigma_p = 1.5$ GeV/c for a neutron momentum of 6.3 GeV/c. A missing perpendicular momentum resolution of about 100 MeV is expected.

The horizontal intersection point of the neutron with the neutron detector will be determined utilizing the time difference between the two phototubes of each neutron detector, while the vertical intersection point will be defined using the segmentation of the neutron detector. A resolution of about 10 cm was achieved in both directions.

4.4.3 Parameters of the Big Ben Magnet

The 48D48 magnet from Brookhaven will be acquired as part of the Super BigBite upgrade and will be available for this experiment. It consists of a large dipole magnet which provides a field integral of about 1.7 T$\cdot$m, allowing for quasielastic protons to be sufficiently deflected to allow clear differentiation from neutrons. The active field volume has an opening of 46×25 cm (vertical $\times$ horizontal), matching the aspect ratio of the neutron arm, and a depth of 48 cm, Fig. 26.

The placement of this magnet will be 1.6 m away from the target, which would normally interfere with the beamline. To accommodate this, modifications will be made to the iron yoke such that the beamline will pass through the magnet itself, Fig. 27. GEANT4 simulations show that the the field within this region will be 70 Gauss over 70 cm, and is small enough such that deflections of the beam towards the beam dump will not be problematic.

The field configuration will be such that positively charged particles will be deflected upwards away from the hall floor. For a field integral of 1.7 T$\cdot$m, protons of momentum 6.3 GeV/c will be deflected 80 mrad, which translates to a displacement of 1.2 m. Including expected detector resolution, the $p_{\text{miss},\perp}$ distribution will be similar to what was seen in E02-013, so cuts of $p_{\text{miss},\perp} < 100$ MeV, will be appropriate. Monte Carlo simulations show a contamination of charged quasielastics to be negligible, Sec. 6.3.

The presence of the magnet also works to sweep low energy charged particles from the target away from the neutron arm. Particles of momentum less than 1.3 GeV will be entirely swept

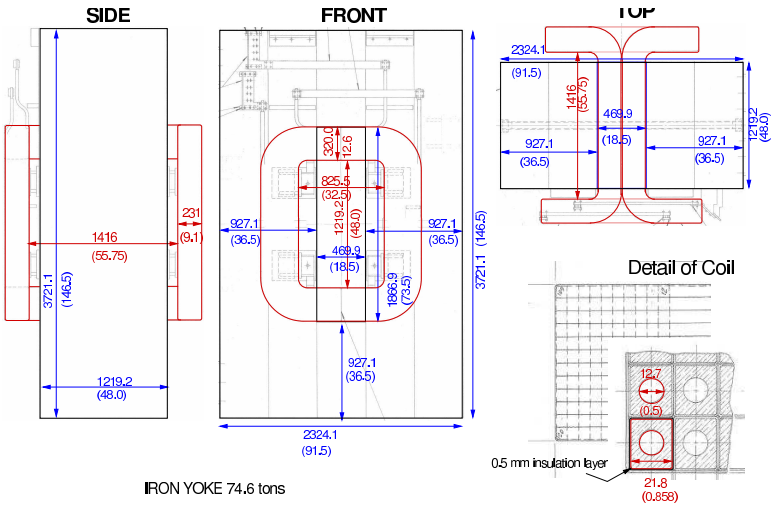

Figure 26: BigBen magnet schematic.

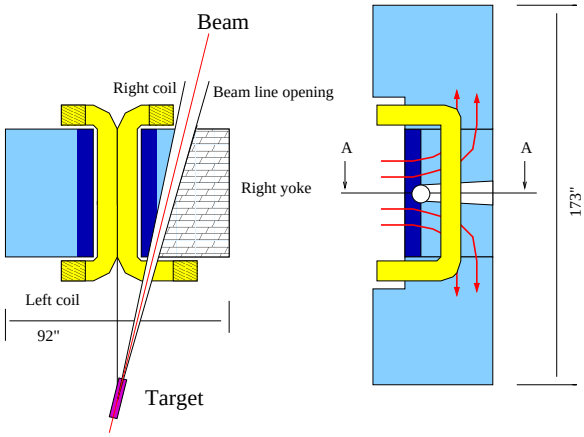

Figure 27: BigBen magnet cuts such that the exiting beamline moves through the magnet.

outside of the neutron arm acceptance. This greatly reduces the amount of charged low energy background.

4.4.4 Expected Background Rates and Shielding

In the proposed experiment the 60 μA electron beam will pass through a 60 cm long ^{3}He target. The total thickness of the glass entrance window is 120 μm and the side window 1.6 mm. A large majority of particles leaving the target in the direction of the neutron arm are photons. For the first G_E^n experiment, which had no such benefit from a magnet, a flux of 3×10^{38} Hz/cm^2 at 7.5 μA. was observed. This corresponded to an observed rate per bar of about 300 kHz. From GEANT simulations, a detector at 17° with a 8.8 GeV beam is expected to have photons rates higher by a factor of four versus a detector at 27° with a 3.2 GeV energy beam. The neutron arm will be further back, reducing the active solid angle by a factor of three and a target of 60 cm instead of 40 cm

will be used. With the addition of the BigBen magnet, the rate will be decreased by an additional factor of 5.

From the first G_E^n experiment, the rate on each neutron arm bar was about 300 kHz given a beam current of 7.5 μA. For our 8.8 GeV^2 beam, we can expect a 1300 kHz rate, or a total flux of 1.3×10^{39} Hz, which, with a nominal TDC deadtime of 50 ns, gives an overall electronic deadtime of 6.5%, within our tolerance.

4.4.5 Veto Detector

Plastic scintillator counters had previously been used to distinguish neutrons from protons. With the addition of the BigBen magnet, this method for identification is no longer necessary. However, these planes will remain in place and can be used for normal hadron detection.

5 Helicity Asymmetry in $^3\vec{\mathrm{He}}(e,e'n)$ and the Ratio of G_E^n/G_M^n

A full analysis of this subject requires calculations which are presently under development in Refs. [71, 72]. Below we summarize the topics which are important ingredients in these calculations or will be used to provide consistency checks and show preliminary results of the calculations from M. Sargsian.

5.1 Nucleons in the Nuclear Medium

There are several processes related to the influence of the nuclear medium on the structure of a bound nucleon. One of the best known is the nuclear EMC effect, which shows that the structure function of the nucleus is suppressed at large x_{Bj} relative to that of the deuteron. While a definitive explanation of this effect is still elusive, it is clear that a quantitative description of the effect requires, in addition to the conventional nucleon and meson degrees of freedom, some dynamical effects involving sub-nucleonic degrees of freedom (see e.g. [73, 74, 75, 76]). However, two factors make the EMC effect controllable in the proposed measurement. First, in models where the EMC effect is proportional to the virtuality of the bound nucleon, which would potentially lead to a distortion of the intrinsic structure of the bound nucleon, the restriction to small values of missing momenta and invariant mass will substantially suppress any such distortion and the corresponding onset of the EMC effect. Secondly, the measured asymmetry will be less sensitive to nucleon structure modifications and the bulk of the EMC effect will be less revealed in the form factor ratios.

Color Transparency (CT) is another effect (see e.g. [77]) which can potentially hinder the extraction of the neutron form factor at high Q^2. This effect has been investigated in quasi-elastic proton knock-out by electrons from nuclei for Q^2 from 1 to 8 GeV^2 [78]. Such studies probe the propagation of the nucleon through nuclei and test the effect of the nuclear medium on the proton knockout cross section. The aforementioned experiment [78] observed no signature for CT up to Q^2=8 GeV^2 in the kinematics of restricted missing momentum and energy. Moreover, the comparison with theoretical calculations demonstrated that the Glauber approximation adequately describes the data for a wide range of nuclei (ranging from the deuteron to iron). Thus for the Q^2 of the present proposal, one expects that the Glauber approximation will reliably describe the final state interactions in the $^3\overrightarrow{\mathrm{He}}(\vec{e},e'n)pp$ reaction.

A study of polarization observables in the reaction $d(\vec{e},e'\vec{p})$ was made at JLab up to $Q^2 =$ 1.6 GeV^2 [79]. Studies of polarization transfers in the reaction ^{4}He($\vec{e}$,e'$\vec{p}$) was also made at Mainz [80] and up to $Q^2 = 2.6$ GeV^2 at JLab [81]. These experiments found that the ratio of the components of the polarization of the recoiling proton P'_x/P'_z can be smaller than the same ratio for a free nucleon target by about 10% (Figs. 28 and 29). The same effects which contribute to this modification need to be taken into account for the analysis of $^3\overrightarrow{\mathrm{He}}(\vec{e},e'n)pp$. The density of a ^{3}He nuclei, which is between the densities of ^{2}H and ^{4}He nuclei, will lead to an averaging of these medium effects. Calculations from J. Udias predict a reduction of the ratio P'_x/P'_z of 8% in ^{4}He compared to hydrogen, whereas in ^{3}He the reduction is only a 4% effect [82].

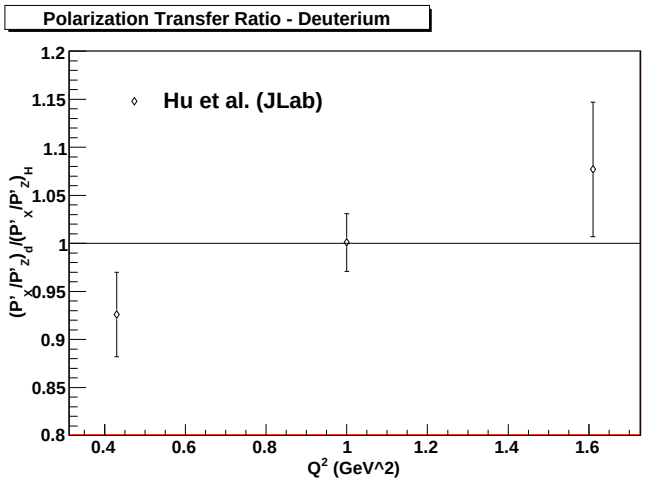

Figure 28: The ratio of the polarization transfer components $(P'_X/P'_Z)_{\mathrm{D}}/(P'_X/P'_Z)_{\mathrm{H}}$ for a bound proton. relative to the free proton [79].

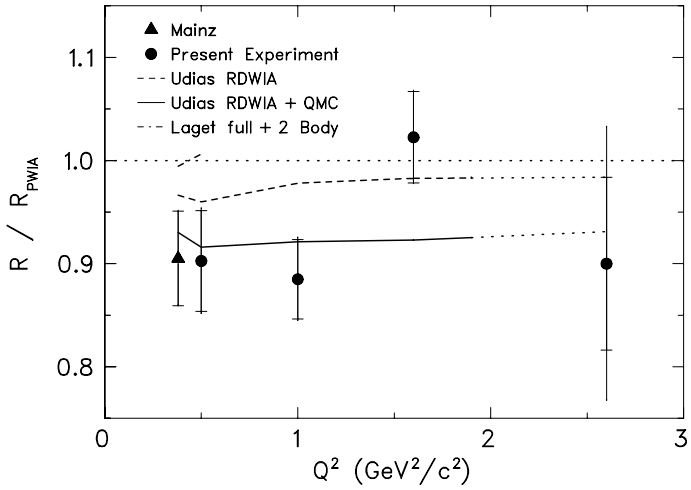

Figure 29: The ratio of the polarization transfer components $(P'_X/P'_Z)_{^4\mathrm{He}}/(P'_X/P'_Z)_{\mathrm{H}}$ for a bound proton. relative to the free proton [81].

5.2 ^{3}He as a Neutron Target

Experiments utilizing ^{3}He targets as effective neutron targets have been carried out for a wide range of beam energies at Bates, Indiana, NIKHEF, Mainz, HERMES, SLAC and, for the last decade, in JLab Hall A. During the past decades there have been several theoretical discussions about the possibility of using a ^{3}He target to study the properties of the elastic electromagnetic form factors of the neutron [10, 57, 83]. In addition, calculations for inclusive and exclusive electron scattering reactions from ^{3}He have been performed [83, 84, 85, 86].

The neutron polarization in ^{3}He and the three-nucleon wave function have been computed by a number of authors using several different methods, including the approach via Faddeev equations [87], and the variational approach [51, 53, 54, 55, 56, 88]. These are now well established, and the error introduced through uncertainty in the wave functions will be very small.

The semi–exclusive reaction $^3\overrightarrow{\mathrm{He}}(\vec{e},e'n)pp$ allows one to fix the values of the missing momenta and energy of the struck neutron which are the key parameters for controlling the size of nuclear effects. A cut on the transverse components of the neutron momentum $p_{\mathrm{miss},\perp}$ is more effective in this task than a cut on the longitudinal component $p_{\mathrm{miss},\parallel}$ [71]. In the proposed experiment the value of the asymmetry will be measured as a function of $p_{\mathrm{miss},\perp}$ in the range 0-100 MeV/c.

5.3 Qualitative Assessments of Nuclear Effects in the Extraction of G_E^n/G_M^n from Semi-exclusive $A(e,e'N)X$ Reactions

The key observation driving the proposed measurement is that it is possible to select small momenta in the ^{3}He wave function by requiring $p_{\mathrm{miss},\perp}<100$ MeV/c. This is the case because the good convergence of the integral $\psi(k)dk$ (normalized as $\int \psi^2(k)d^3k = 1$) leads to the selection of very small momenta in the wave function of ^{3}He, even though the cut on $p_{\mathrm{miss},\parallel}$ is rather large (1.5 GeV/c).

Additionally, these suppress small non-nucleonic admixtures in the wave function and they significantly suppress the final state interactions, since the struck nucleon is rather far from other nucleons. Most of the rescattering in these kinematics moves nucleons to larger $p_{\mathrm{miss},\perp}$ and hence they do not greatly affect asymmetries calculated in the PWIA in order to extract $R = G_E^n/G_M^n$.

The following is the assessment of nuclear effects that may affect this extraction, and some qualitative estimations indicating which corrections will be possible to estimate more quantitatively.

1. Finite acceptance effects. Because the experiment will measure G_E^n within a finite interval of missing momenta p_{miss}, the integration will smear out the extracted R. An averaging scheme where $A_\perp$ and $A_\parallel$ are expanded out in powers of the ratio G_E/G_M developed for the previous G_E^n experiment will be used [89].

2. Off-shell effects. The uncertainty associated with off-shell effects can be estimated by applying the different off-shell prescriptions for calculation of nucleon currents. However, since the momenta of the struck nucleons are small, these effects, which are proportional to p_m^2/m_N^2, should be strongly suppressed.

3. Meson Exchange Effects. The choice of high Q^2 causes a significant suppression of meson exchange effects in the extraction of R. At $Q^2 > 1$ GeV^2 the overall additional Q^2 dependence

of the MEC amplitude as compared to the PWIA amplitude will be $(1+Q^2/\Lambda^2)^{-2}$, where $\Lambda^2 = 0.8-1$ GeV^2 (see e.g. [71]).

4. Delta Isobar Contribution. This effect should be small because of the restrictions on $p_{\rm miss}$. If one assumes the same Q^2 and energy dependence of the elastic electromagnetic form factor as of the $N\Delta \to NN$ rescattering amplitude, one is able to estimate the Δ contribution using the FSI amplitude but taking into account the fact that it corresponds to the larger $p_{{\rm miss},\|}$ in the argument of the nuclear wave function. This gives the upper limit of the Δ contribution.

   Pre-existing Δ-isobars in ^{3}He have a rather small probability – about 2% – and they also have substantially larger average transverse momenta than nucleons. Hence the cut on small average nucleon momenta will lead to further suppression. This is a potential background since there can be a transition $\gamma^*\Delta^0 \to n$. From the violation of the Bjorken sum rule one can expect the Δ contribution integrated over all momenta to be on the level of 4% times the ratio of the ΔN form factor and the NN form factor. An additional small factor mentioned above is the cut on momenta – so qualitatively one may get an effect on the scale of 1-2%.

5. Final State Interactions. The major advantage is that at high Q^2 the eikonal approximation is applicable when the rescattering amplitude is practically energy-independent. First we discuss FSI due to diagonal $np \to np$ rescattering. In the case of the factorized approximation the uncertainty comes from the accuracy of the calculation of FSI contributions, which is less than 10%. The comparison of eikonal calculations with JLab data demonstrated very good agreement for Nuclear Transparency starting with the deuteron and going up to iron [78].

   In the case of small $p_{{\rm miss},\perp}$, the overall effect of FSI for the ^{3}He target is about 10%, thus the uncertainty due to the accuracy of FSI is 1-1.5%. The theoretical calculations will allow an estimate of this contribution.

   Calculations regarding these effects for ^{3}He at high Q^2 are currently underway by J. M. Laget and M. Sargsian. We anticipate having results regarding these effects by the end of January 2009.

To summarize, it appears that corrections to the impulse approximation will be significantly less than 10% (expected on the level of 2-5%), and most of these effects will be possible to correct for.

5.4 Preliminary Results of the GEA Calculation

GEA [71], a code based on the generalized eikonal approximation, was used for the calculations of $A_\perp$ shown in Fig. 30. The asymmetries were calculated for a beam energy of 3.244 GeV and assuming that G_E^n follows the Galster parameterization. The following cuts on the components of missing momenta were applied: $p_{{\rm miss},\perp}$ less than 50 MeV/c and $p_{{\rm miss},\|}$ less than 250 MeV/c. The invariant mass cut was $W = 0.94 \pm 0.05$ GeV. The upper solid line presents the results of the code for a free neutron at rest. The lower solid line with smaller values of $A_\perp$ is a naive estimate of the asymmetry based on the neutron carrying 86% of the polarization of ^{3}He. The dash line presents the results of the PWIA calculation. The dotted line is the results of the DWIA calculation. The dash-dotted line presents the DWIA calculation with Charge Exchange (CE) effects included. The effect of CE is about 5.5% at Q^2= 1 GeV^2 and drops to 3.6% at Q^2= 4 GeV^2 , in agreement with

our expectations. A complete version of this code to evaluate at higher Q^2 is expected to become available soon.

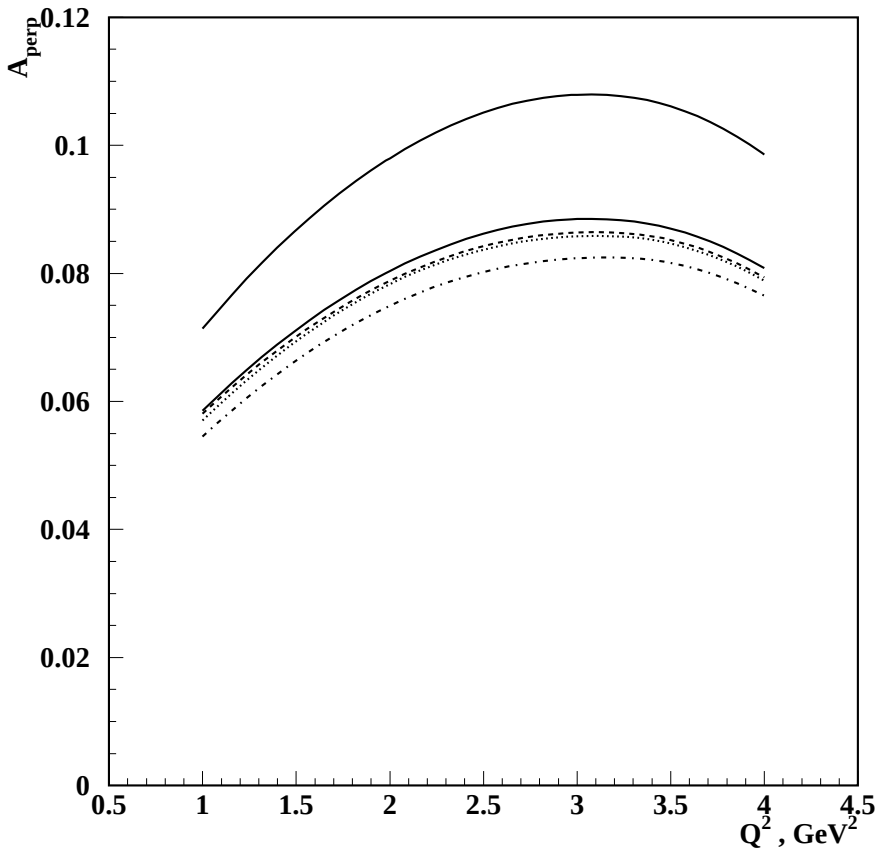

Figure 30: The $A_\perp$ asymmetry calculated by Sargsian [71] in the generalized eikonal approximation. The upper solid line presents the result for a free neutron at rest. The lower solid line with smaller value of $A_\perp$ is a naive estimate of the asymmetry based on the neutron carrying 82% of the polarization of ^{3}He. The dash line presents the results of the PWIA calculation. The dotted line is the results of the DWIA calculation. The dash-dotted line presents the DWIA calculation with CE effects included.

6 Quasi-Elastic Scattering at Q^2 of Several GeV^2

In this section we will discuss the physics and background contributions to the data and the method of separating the quasi-elastic scattering (QES) events from the background. Several physics processes contribute to the background which the detectors will see, including inelastic scattering associated with pion electroproduction and quasi-elastic scattering from the protons in ^{3}He. Inelastic scattering associated with pion production will be discussed in the first subsection. Charged pions overlapping electrons in BigBite can be suppressed by using particle identification, as discussed in the second subsection. The suppression of quasi-elastic scattering from the protons in ^{3}He will be performed magnetically and will be discussed in the third subsection. The accidental background in the data comes from accidental coincidences due to the high rates of low energy photons, neutrons, and pions, which will be discussed in Sec. 6.4.

6.1 Selection of the QES Events

The first step of an extraction of G_E^n is the selection of the quasi-elastic scattering events. The previous G_E^n experiment used MC simulations of QES and pion production to evaluate background contributions.

From the previous experiment, we examine data from $Q^2 = 1.7$ and 3.5 GeV^2. Quasielastic events were selected by placing cuts on $p_{\mathrm{miss},\perp}$, $p_{\mathrm{miss},\parallel}$, m_{miss}, and a pseudo-invariant mass where the initial nucleon is assumed to be at rest. This invariant mass correlates very closely with x_{bjk}. For these measurements, separation between the quasielastic events and inelastic background can be seen, Figs. 31 and 32. For the preliminary analysis of this experiment, cuts were placed conservatively to eliminate the dependence on corrections from Monte Carlo simulations.

We rely on tight cuts on $p_{\mathrm{miss},\perp}$ to suppress larger contributions from final state interactions. For this experiment, we anticipate the $p_{\mathrm{miss},\perp}$ distribution be be similar to that seen in E02-013, Fig. 33. By placing similar cuts at 100 MeV, we also help separation from inelastic contributions.

For our proposed kinematics, this separation is not expected to be as clean due to a $p_{\mathrm{miss},\parallel}$ resolution of $\sigma = 1.5$ GeV/c, close to a factor of 10 worse. Because of the $p_{\mathrm{miss},\parallel}$ resolution, cuts on missing mass will be ineffective at removing pions production events near threshold. However, placing cuts on $p_{\mathrm{miss},\parallel}$ will still be useful in eliminating background and events where the nucleon had additional interactions before reaching the neutron arm. In light of this, it will be critical to make a correction on the asymmetry.

For the cross section, one can use DIS or exploit quark hadron duality. The asymmetry will be obtained in the data. By assuming small variations in the observed asymmetry across scales of the invariant mass width due to Fermi smearing, a deconvolution between the elastic and inelastic asymmetries can be performed. Such a method would have proved to have been successful in the E02-013 data. In this data, a smooth variation of the asymmetry between quasielastic and inelastic dominated regions was seen, Fig. 34. This deconvolution can be performed through a maximum likelihood method where the likelihood for an observed asymmetry is given by

$$f(A_i|A_{\mathrm{inelas}},A_{\mathrm{elas}},\alpha_i,N_i) = \exp\left[-\frac{N_i\left(A_i-\alpha_i A_{\mathrm{elas}}-(1-\alpha_i)A_{\mathrm{inelas}}\right)^2}{2(1-A_i^2)}\right], \tag{22}$$

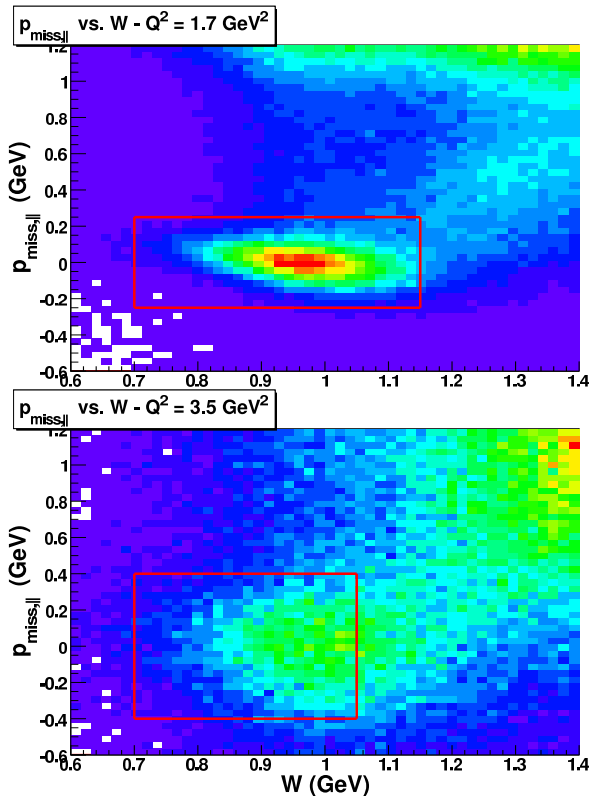

Figure 31: $p_{\mathrm{miss},\parallel}$ vs. W from ^{3}He for E02-013, (top) $Q^2 = 1.7$ GeV^2 and (bottom) $Q^2 = 3.5$ GeV^2.

where A_i is the observed asymmetry in the ith bin, where the bin is some arbitrary subset of data, A_{inelas} and A_{elas} are the inelastic and elastic asymmetries, N_i is the number of statistics in the bin, and α_i is the fraction of statistics that are (quasi)elastics. α_i for each bin will be determined by a Monte Carlo simulation.

To find the parameters A_{inelas} and A_{elas}, one solves the equations given by

$$0 = \frac{\partial \ln \mathcal{L}}{\partial A_x} = \frac{\partial \ln \left(\prod_i f(A_i)\right)}{\partial A_x}, \tag{23}$$

for asymmetry A_x where x is inelas or elas. This analysis will utilize bins across $p_{\mathrm{miss},\perp}$ and W^2, where higher $p_{\mathrm{miss},\perp}$ values are dominated by inelastics. W^2 will be kept below two pion production such that the same production channels as at lower W^2 will be selected.

Contributions from inelastics for our cuts will be on the order of 25%, Fig. 35. Cuts on $p_{\mathrm{miss},\perp}$ are more severe than used in E02-013 due to the higher inelastic background rates, Fig. 36. As we are only interested in inelastic events within only a couple hundred MeV of the quasielastic peak, production of more than one pion is highly suppressed. For the previous G_E^n data, parameterizations of single pion production cross sections and asymmetries from MAID were available so such a deconvolution technique was not necessary.

From local quark-hadron duality in spin dependent observables, constraints can be made regarding the asymmetry contributions. Quark-hadron duality has been shown for polarized ^{3}He structure

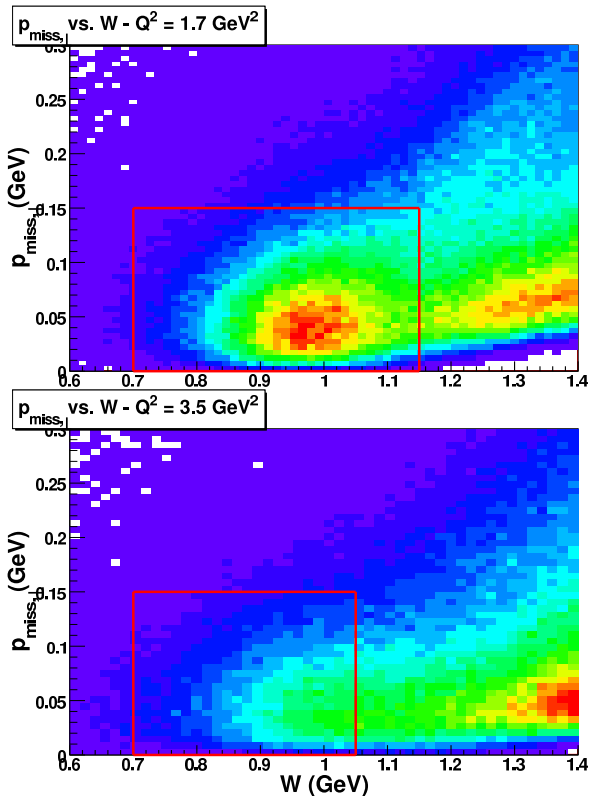

Figure 32: $p_{\mathrm{miss},\perp}$ vs. W from ^{3}He for E02-013, (top) $Q^2 = 1.7$ GeV^2 and (bottom) $Q^2 = 3.5$ GeV^2.

functions g_1 for Q^2 of at least 2 GeV^2 and global duality in g_2 down to $Q^2 = 1$ GeV^2 [90, 91, 92, 93]. At higher Q^2, duality is expected to hold more strongly.

From E02-013, this asymmetry was found to be the same sign and within a factor of two smaller than the quasielastic asymmetry for all Q^2 points, Fig. 34. The quasielastic asymmetry will become smaller by about a factor of two for $Q^2 = 10$ GeV^2. The range in x_{bjk} for the E02-013's $Q^2 = 3.5$ GeV^2 point and this proposal's $Q^2 = 10$ GeV^2 point both range from $x = 0.93$ to $x = 1$, allowing for explicit use of quark-hadron duality in spin observables. From this, it is reasonable to estimate that the inelastic asymmetry contributions will be within a factor of two of the quasielastic asymmetry.

As inelastic events are anticipated to contribute about 25% of the statistics to the quasielastic sample, an inelastic asymmetry a factor of two different than the quasielastic asymmetry will require a correction on the order of $15 \sim 30\%$. Inelastic asymmetry values near that of the quasielastic asymmetry would require much smaller corrections. We anticipate that we will be able to determine the correction to within 5% relative to the value of the asymmetry through the deconvolution method described above.

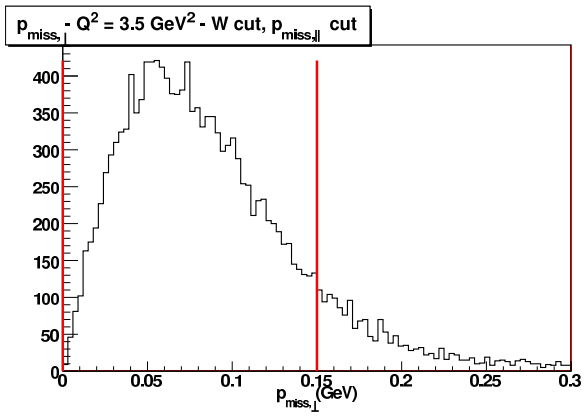

Figure 33: $p_{\mathrm{miss},\perp}$ from ^{3}He for E02-013, $Q^2 = 3.5$ GeV^2.

6.2 Pions in BigBite

The contribution of pions in the electron arm can be evaluated using a parameterization of the charged pion cross sections [69]. As the scattering events of interest are quasielastic, they are typically of the highest energy. However, due to Fermi-smearing, the difference in momentum observed in BigBite from the momentum that would be expected from elastic scattering has a half width of approximately 300 MeV. Use of this parameterization shows that the number of pions to electrons is expected to be about 3:1. Through use of the preshower calorimeter and gas Cerenkov, a total pion rejection factor of 10^4 is expected. Unrejected pions could only contribute less than 0.1% to the physical asymmetry, A_{phys}, which is negligible for our anticipated error.

The background from the glass windows of the target cell and other windows will be cut out in the analysis by using cuts on the reconstructed vertex along the target.

6.3 Quasielastics from the Protons in ^{3}He

The rate of quasielastics from the bound protons in ^{3}He is about factor of 12 higher than in the process under study neglecting the relative detection efficiency between protons and neutrons. Protons with momentum 6.3 GeV/c will be shifted 1.2 m on the face of the neutron arm allowing for cuts on $p_{\mathrm{miss},\perp}$ to primarily provide proton/neutron differentiation. Due to finite resolution and the natural width of $p_{\mathrm{miss},\perp}$, there will be some overlap between the two. For the expected magnetic separation contributions of protons will be negligible with our anticipated cuts of $p_{\mathrm{miss},\perp}$ of 100 MeV 37.

6.4 Accidental Background

Overall background rates in the neutron arm are expected to be about two or three times that seen in the first G_E^n experiment. For that analysis, neutron arm hits with reconstructed $\beta > 1$ were shifted in time by a constant chosen such that the quasielastic region would be entirely populated by only accidental background. This produces a set of data with an accidental background rate and distribution identical to the experimental conditions. By applying an identical set of cuts to the shifted data, the contributions from accidental background can be accurately quantified.

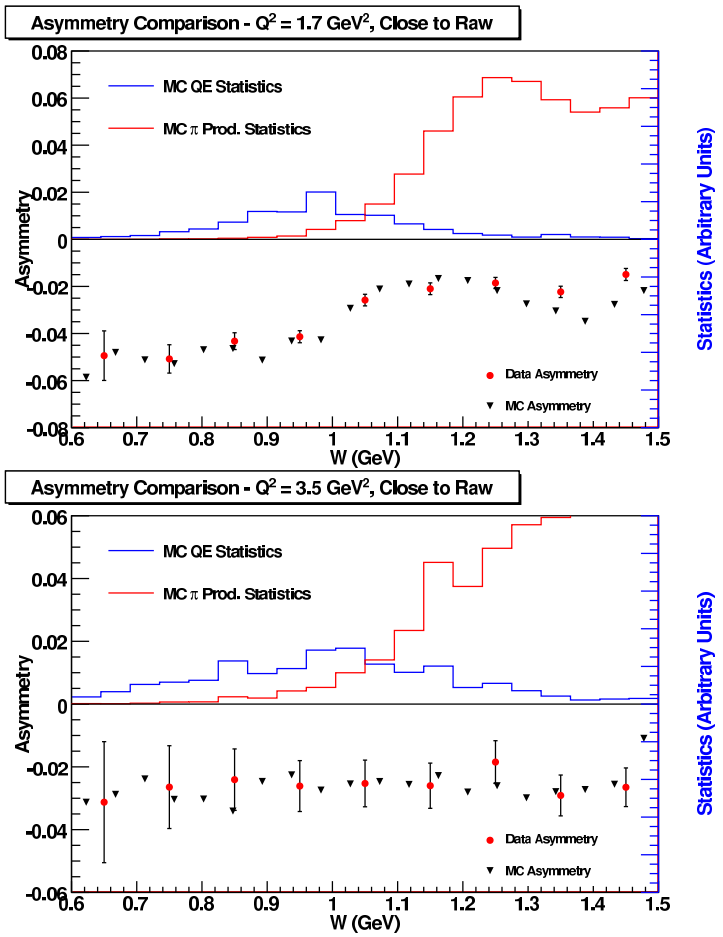

Figure 34: Helicity dependent asymmetry from E02-013 at $Q^2 = 1.7$ (top) and 3.5 GeV^2 (bottom) vs. invariant mass with large cuts. Asymmetry and cross section values from MAID agree very well with data.

For the previous G_E^n experiment, the overall background contributions were found to be $1-2\%$ for neutron arm bar rates of 400 kHz. These events will then contribute only $2-6\%$, which should present no difficulty for the analysis.

6.5 Analysis of the Corrected Asymmetry and Extraction of G_E^n/G_M^n

After obtaining the asymmetry, A_{phys}, corrected for background and polarizations, contributions from both $A_{\parallel}$ and $A_{\perp}$ must be separated in through some method due to the large angular acceptance of the electron arm. Through a power expansion of A_{phys} in terms of the ratio G_E/G_M to sufficient order, the problem reduces to solving a polynomial of finite order. This method was used for E02-013 and is described in [89]. Since G_E/G_M is small, an expansion to 5th order will be sufficient. The systematics of the $A_{\parallel}$ calculation are expected to be less than 0.001 for an angular alignment accuracy of 1 mr.

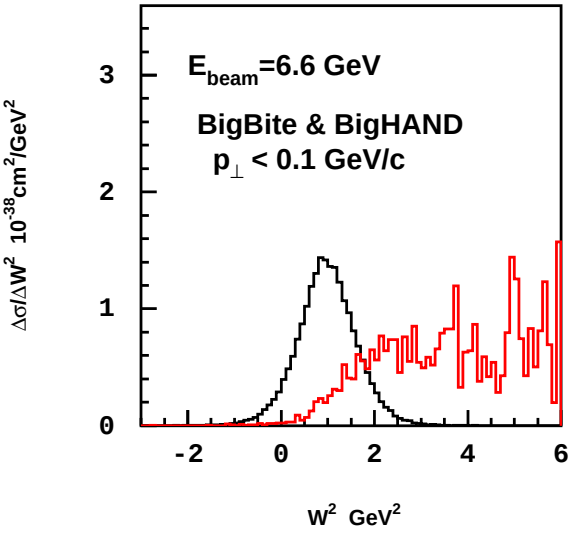

Figure 35: Quasielastic and inelastic contributions for $Q^2 = 6.8$ GeV^2 (top) and $Q^2 = 10$ GeV^2 (bottom) with cuts on $p_{\mathrm{miss},\perp} < 100$ MeV.

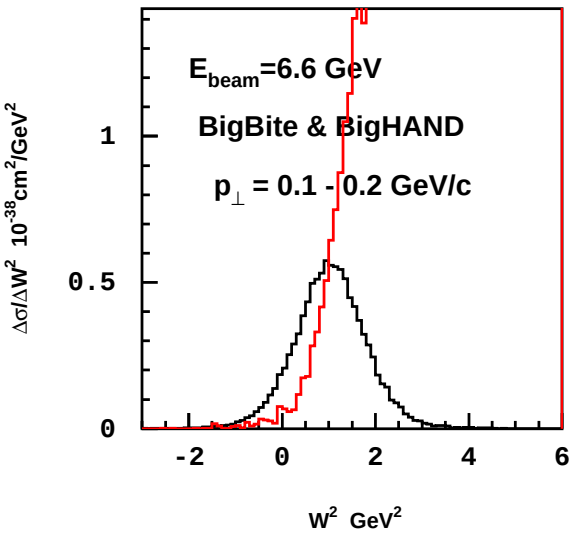

Figure 36: Quasielastic and inelastic contributions for $Q^2 = 6.8$ GeV^2 (top) and $Q^2 = 10$ GeV^2 (bottom) with cuts on $100 < p_{\mathrm{miss},\perp} < 200$ MeV.

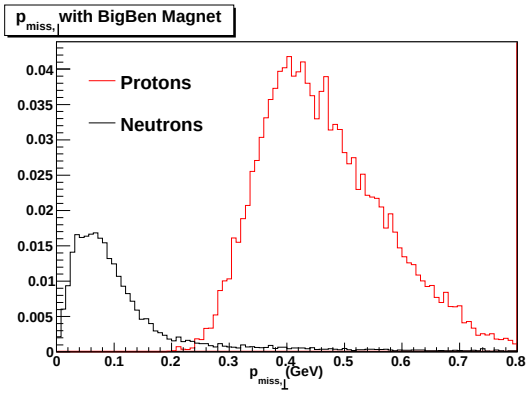

Figure 37: Neutron and deflected proton quasielastic distributions in $p_{\text{miss},\perp}$ at $Q^2 = 10$ GeV^2. Cuts near 100 MeV will sufficiently eliminate quasielastic proton contributions.

7 Proposed Measurements

7.1 Kinematics

To choose which is the best combination of beam energy and scattering angle to measure G_E^n for a given Q^2, one has to evaluate the figure-of-merit (FOM). In our case, the FOM is given by

$$FOM = \frac{R(\theta)}{1 - A_{\text{exp}}^2}, \tag{24}$$

where $R(\theta)$ is the counting rate, which itself is proportional to the product of the cross section, the effective target length, the beam current, and the acceptance of the particular spectrometers used. In Fig. 38 the FOM is plotted as function of the beam energy at a fixed Q^2 of 10 GeV^2. To study the influence of the value of G_E^n itself, the FOM has been calculated assuming that G_E^n follows the variations of the Galster parameterization. For a given Q^2, the FOM increases for higher beam energies, which corresponds to detecting the electron at smaller scattering angles. The variation of G_E^n does not change the general behavior of the FOM.

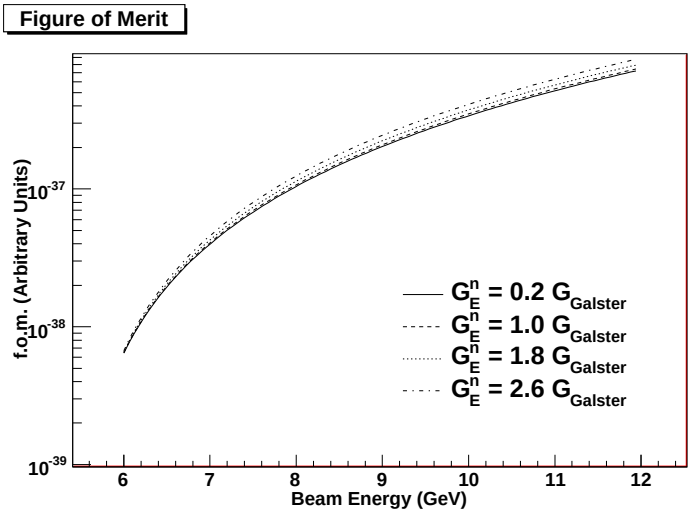

Figure 38: The FOM as function of the beam energy at fixed $Q^2 = 10.0$ GeV^2. An increase in the beam energy translates into smaller electron scattering angles and higher momenta of the recoiled electron.

The minimum angle that BigBite may be set to without technical difficulty is about 34°, which corresponds to the available beam energy of 8.8 GeV. The other two kinematics were chosen to provide about 40% higher Q^2 from the prior point. Table 1 summarizes the proposed kinematics.

7.2 Asymmetry and Rate Estimates

The asymmetry A_{phys} in $e-n$ scattering is related to the experimentally measured asymmetry $A_{\text{exp}} = (N_+ - N_-)/N$ via the equation

$$A_{\text{phys}} = \frac{A_{exp}}{P_{\text{beam}} P_{^3\text{He}} P_n D_{\text{N}_2} D_{\text{FSI}} D_\pi D_{\text{back}}}, \tag{25}$$

Q^2 (GeV^2)	E_i (GeV)	θ_e (deg)	p_e (GeV/c)	θ_n (deg)	p_n (GeV/c)
5.02	4.400	48.0	1.73	21.6	3.49
6.77	6.600	34.0	3.00	22.2	4.44
10.18	8.800	34.0	3.38	17.5	6.29

Table 1: The three proposed kinematics.

where the values of the various polarizations and dilutions can be found in Table 3.

The following rate estimates are based on scattering from a free neutron using $G_E^n = G_{\rm Galster}$ and G_M^n from a parameterization by Kelly [27]. Radiative corrections further reduce the number of useful events by roughly 10%.

Q^2 (GeV^2)	rate (Hz)	$A_{\rm exp}$	G_E^n/G_M^n
5.02	0.146	-0.0581	-0.1770
6.77	0.081	-0.0547	-0.1918
10.18	0.010	-0.0292	-0.2098

Table 2: Rate estimates for this proposal. We assume a target polarization $P_{^3\rm He}$ of 60%, a beam polarization $P_{\rm beam}$ of 85% an average beam current of 60μA, a viewable target length of 55 cm, and a solid angle of 44 msr for the electron arm. Furthermore, this rate is calculated assuming that we detect the neutrons with an efficiency of 90% and cuts reduce statistics by 75%.

To help minimize the contribution of inelastic background, we used a Monte Carlo to evaluate that these cuts will reduce the number of statistics to about 25%, Fig. 39. This Monte Carlo was used to reproduce data seen in experiment E02-013, Fig. 40. The anticipated rates and asymmetries using these assumptions, are shown in Table 2.

7.3 Error Estimates and Beam Time Request

The uncertainty $\delta A_{\rm phys}$ can be expressed as

$$\left(\frac{\delta A_{phys}}{A_{phys}}\right)^2 = \left(\frac{\delta A_{exp}}{A_{exp}}\right)^2 + \sum\left(\frac{\delta P_i}{P_i}\right)^2 + \sum\left(\frac{\delta D_i}{D_i}\right)^2, \tag{26}$$

where the sums run over all the contributions of polarizations and dilutions. The beam polarization in Hall A can be measured with the Compton and the Møller polarimeter to better than 2%. Both polarimeters are standard equipment in Hall A. The polarization of ^{3}He can be measured with a relative uncertainty of 4%, the polarization of the neutrons in ^{3}He is known to 2%.

The statistical uncertainty is $\delta A_{\rm exp,stat} = sqrt(1-A_{\rm exp}^2)/N$. To extract G_E^n from the measured $A_{\rm phys}$, Eq. 13 has to be evaluated. Investigating the error propagation in this equation, taking an expansion of $A_{\rm phys}$ in G_E^n/G_M^n to first order gives

$$\delta\left(\frac{G_E^n}{G_M^n}\right) = \delta A_{\rm phys}\frac{2\sqrt{\tau(1+\tau)}\tan(\theta/2)\sin\theta^*\cos\phi^*}{\tau+2\tau(1+\tau)\tan^2(\theta/2)}. \tag{27}$$

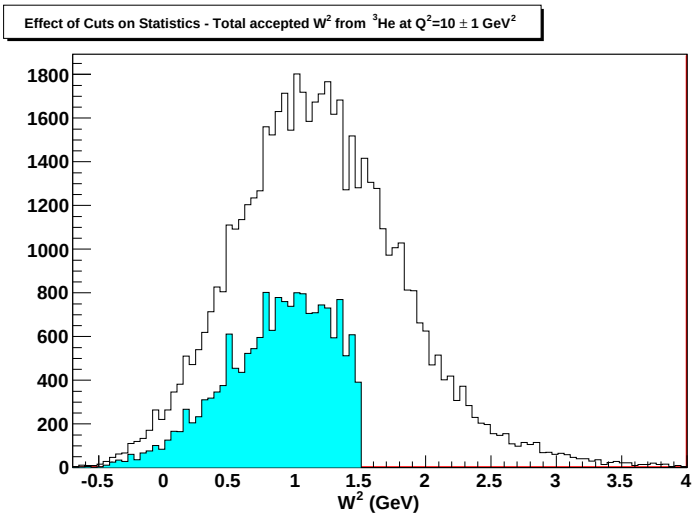

Figure 39: Effect of proposed cuts on statistics for simulated ^{3}Hedata at 10 GeV^2. The shaded region represents the data after cuts of $p_{\mathrm{miss},\perp} < 100$ MeV, $W^2 < 2$ GeV^2, and $-p_{\mathrm{miss},\parallel}- < 1.5$ GeV.

As discussed in Sec. 5, we expect the correction factor D_{FSI} for nuclear effects to be 0.85 – 1.0, and the corresponding systematic error to be about 5%. Table 3 summarizes the various contributions to the total error for the example of the highest Q^2 point.

Quantity	Expected Value	Rel. Uncertainty
Statistical error	0.0292	19.9%
Beam polarization P_e	0.85	2.4%
Target polarization $P_{^3\mathrm{He}}$	0.60	3.3%
Neutron polarization P_n	0.86	2.3%
Nitrogen dilution D_{N_2}	0.94	2.1%
Background dilution D_{back}	0.95	$< 1\%$
Final state interactions	0.95	5.3%
Inelastic correction	0.8-1.2	5.0%
Angular error from $A_{\parallel}$		$< 1\%$
Statistical error in G_E^n/G_M^n		18.1%
Systematic error in G_E^n/G_M^n		7.7%

Table 3: The various contributions to the total error in G_E^n for the data point at Q^2=10.0 GeV^2.

One purpose of this experiment is to measure the ratio G_E^n/G_M^n with an uncertainty similar to the results on G_E^n/G_M^n achieved in E02-013. Therefore our beamtime request is chosen so that we can obtain a statistical uncertainty $\Delta(G_E^n/G_M^n) < 0.20$. The resulting times are summarized in Table 4.

The polarization measurements, besides the Compton measurement, are disruptive, so additional beamtime is needed. To monitor the target polarization continuously, one target polarization measurement every six hours is necessary. Also, the Møller polarization measurements need additional time. To measure the dilution from nitrogen, the reference target cell will be filled with nitrogen. Additionally, H_2 and carbon foil/sieve data will be taken at each momentum setting

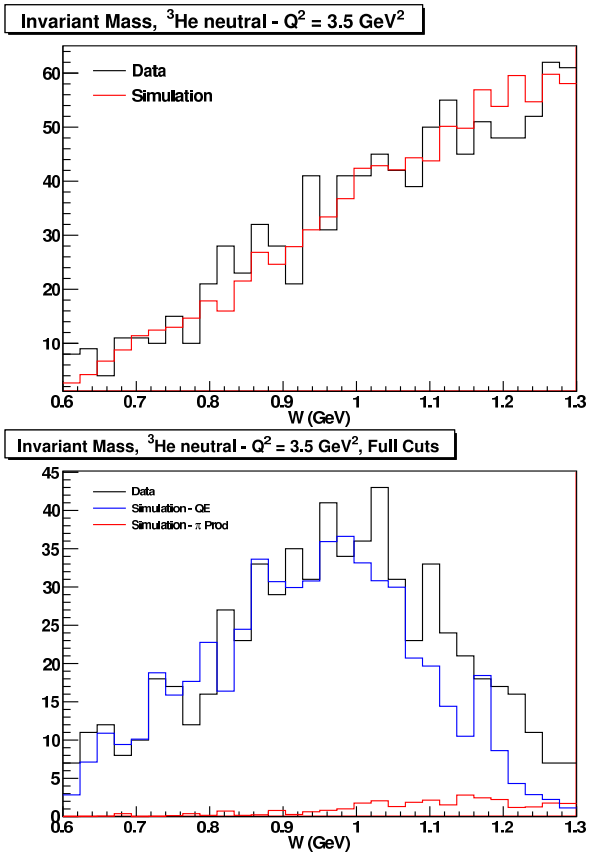

Figure 40: E02-013 Monte Carlo results for invariant spectra at $Q^2 = 3.5$ GeV^2. The spectra are reproduced well for (top) near raw and (bottom) full quasielastic cuts.

to help calibrate the BigBite optics. We expect an overhead of 20% for these studies. During the experiment, two configuration changes are necessary. These changes include a change of the beam energy, changes of the position neutron detector array, and adjustments or replacement of the polarized ^{3}He target. Each configuration change will take approximately one shift. We furthermore request 48 hours of beamtime for initial calibration runs. In total we request 1384 hours of beamtime to perform the proposed measurement, as detailed in Table 5.

Q^2 (GeV^2)	time (hours)	Counts	G_E^n/G_M^n	stat. err.	sys. err.	G_E^n (Galster)	ΔG_E^n (G_M^n known)
5.02	38	20209	-0.1770	0.0319	0.0222	0.0046	0.0010
6.77	154	44928	-0.1918	0.0259	0.0253	0.0028	0.0005
10.18	864	29651	-0.2098	0.0380	0.0161	0.0014	0.0003

Table 4: Expected uncertainties for this proposal. The times given in this table are pure data taking times assuming 100% efficiency. They do not include the time needed for polarization measurements, optics data, or measurements of the dilution factor, D_{N}. The number of counts is given for the cuts described in the text.

	Beam Energy (GeV)	Data Taking Time (hours)	Total Time (hours)
Calibration Runs	4.400		48
$Q^2 = 5.0$ GeV^2	4.400	38	48
$Q^2 = 6.8$ GeV^2	6.600	154	192
$Q^2 = 10.2$ GeV^2	8.800	864	1080
Configuration Changes			16
Total		1055	1384

Table 5: Beamtime request for this proposal, assuming 100% availability of the accelerator and the experimental equipment. Data taking time includes only the time for measuring G_E^n, whereas the total time also includes the time needed for polarization measurements, optical calibrations, and measurements of the dilution factor, D_{N_2}.

8 Conclusions

We request 1386 hours to measure G_E^n at Q^2=5.0, 6.8, and 10.2 GeV^2 through a measurement of the cross section asymmetry of the reaction $^3\overrightarrow{\mathrm{He}}(\vec{e},e'n)pp$. This experiment will take place in Hall A, utilizing the BigBite spectrometer to detect electrons scattered off the Hall A polarized ^{3}He target, and an array of scintillators to detect the recoiling neutron. There are no other measurements of G_E^n at these momentum transfers and knowledge of the neutron electric form factor G_E^n is essential for the understanding of the nucleon structure. Furthermore, it is a necessary input in the analysis and interpretation of processes involving the electromagnetic interaction with nuclei. We propose to measure G_E^n/G_M^n to an accuracy of $\Delta G_E^n/G_M^n$= 0.06, which would bring its precision to a level comparable with that of the other Sachs form factors in this kinematical regime.

The kinematics of our measurements emphasize the same Q^2 range studied for the proton. For these large momentum transfers it was found that the charge and magnetic current distributions in the proton are markedly different at short distances. It is an intriguing question to see if a similar tendency is duplicated in the neutron. Furthermore, pQCD made clear predictions on how these form factors should scale at arbitrarily high Q^2. Measuring at relatively high momentum transfers will also open additional dimensions for testing the models of the nucleon form factors in the generalized parton distribution framework.

References

[1] J. J. Kelly, Phys. Rev. C **66** 065203 (2002)

[2] M. Jones *et al.*, Phys. Rev. Lett. **84** , 1398 (2000).

[3] O. Gayou *et al.*, Phys. Rev. Lett. **88**, 092301 (2002).

[4] V. E. Krohn and G. R. Ringo, Phys. Rev. **148**, 1303 (1966).

[5] L. Koester, W. Nistler, and W. Waschkowski, Phys. Rev. Lett. **36**, 1021 (1976).

[6] A. I. Akhiezer, L. N. Rozensvaig and I. M. Shmushkevich, JETP **33**, 765 (1957).

[7] N. Dombey, Rev. Mod. Phys. **41**, 236 (1969).

[8] A. I. Akhiezer and M. P. Rekalo, Sov. J. Part. Nucl. **3**, 277 (1974).

[9] R. Arnold, C. Carlson, and F. Gross, Phys. Rev. **C 23**, 363 (1981).

[10] B. Blankleider and R. M. Woloshyn, Phys. Rev. **C 29**, 558 (1984).

[11] M. Meyerhoff *et al.*, Phys. Lett. B **327**, 201 (1994).

[12] J. Becker *et al.*, Eur. Phys. J, A **6**, 329 (1999).

[13] D. Rohe *et al.*, Phys. Rev. Lett. **83**, 4257 (1999).

[14] J. Bermuth, *et al.*, Phys. Lett. B **564** (2003) 199.

[15] I. Passchier *et al.*, Phys. Rev. Lett. **82**, 4988 (1999).

[16] C. Herberg *et al.*, Eur. Phys. J. **A5**, 131 (1999).

[17] M. Ostrick *et al.*, Phys. Rev. Lett. **83**, 276 (1999).

[18] E. Geis, *et al.*, Phys. Rev. Lett. **101**, 042501 (2008)

[19] R. Madey, *et al.*, Phys. Rev. Lett. **91**, 122002 (2003).

[20] G. Warren, *et al.*, Phys. Rev. Lett. **92**, 042301 (2004).

[21] D. Glazier *et al.*, Eur. Phys. J. **A 24**, 101 (2005).

[22] R. Schiavilla and I. Sick, Phys. Rev. C **64** 041002 (2001).

[23] S. Galster *et al.*, Nucl. Phys. B **32**, 221 (1971).

[24] J. Lachniet, Ph.D. Thesis, Carnegie Mellon University, Pittsburgh, PA, USA (2005).

[25] J. Lachniet, *et al.*, arXiv:0811.1716

[26] S. Rock, *et al.*, Phys. Rev. D **46**, 24 (1992).

[27] J.J. Kelly, Phys. Rev. C 70 (2004) 068202

[28] M. A. Shupe *et al.*, Phys. Rev. D **19**, 1929 (1979).

[29] G. Miller, Phys. Rev. Lett. **99**, 112001 (2007).

[30] C. Carlson and M. Vanderhaeghen, Phys. Rev. Lett. **100**, 032004 (2008).

[31] L. Andivahis *et al.*, Phys. Rev. D **50**, 5491 (1994).

[32] R. G. Arnold *et al.*, Phys. Rev. Lett. **57**, 174 (1986);
A.F. Sill *et al.*, Phys. Rev. D **48**, 29 (1993).

[33] S. J. Brodsky and G. Farrar, Phys. Rev. Lett. **31**, 1953 (1973).

[34] S. J. Brodsky and G.P. Lepage, Phys. Rev. D **22**, 2157 (1981).

[35] A.V. Belitsky, X.D. Ji, F. Yuan, Phys. Rev. Lett. **91** 092003 (2003).

[36] S. Riordan, Ph.D. Thesis, Carnegie Mellon University, Pittsburgh, PA, USA (2008).

[37] M .S. Bhagwat, I. C. Cloet, C. D. Roberts, arXiv:0710.2059 [nucl-th]

[38] X. Ji, Phys. Rev. D **55**, 7114 (1997); Phys. Rev. Lett. **78**, 610 (1997).

[39] A.V. Radyushkin, Phys. Lett. B **380**, 417 (1996).

[40] A.V. Radyushkin, Phys. Rev. D **56**, 5524 (1997).

[41] M. Diehl, T. Feldmann, R. Jakob, and P. Kroll, arXiv:hep-ph/0408173

[42] P. Kroll, arXiv:hep-ph/0612026v1

[43] M. Guidal, M.V. Polyakov, A.V. Radyushkin, and M. Vanderhaeghen, arXiv:hep-ph/0410251v1

[44] A.V. Radyushkin, Phys. Rev. D **58**, 114008 (1998).

[45] M. Diehl, T. Feldmann, R. Jakob, and P. Kroll, Eur. Phys. J. C **8**, 409 (1999).

[46] P. Kroll, PiN Newslett. **15**, 205 (1999).

[47] K. Goeke, M. V. Polyakov, and M. Vanderhaeghen, Prog. Part. Nucl. Phys. **47**, 401 (2001).

[48] J. Ralston, P. Jain and R. Buney, Proceedings of the Conf. on Intersections of Particle and Nuclear Physics, Québec City, (2000), ed. Z. Parseh and M. Marciano, AIP Conf. Proc. No. 549 (AIP, New York, 2000), p. 302.

[49] T. W. Donnelly and A. S. Raskin, Ann. Phys. (N.Y.) **169**, 247 (1986).

[50] A. S. Raskin and T. W. Donnelly, Ann. Phys. (N.Y.) **191**, 78 (1989).

[51] C. Ciofi degli Atti, and S. Scopetta, Phys. Lett. B **404**, 223 (1997).

[52] R. M. Woloshyn, Nucl. Phys. A **496**, 749 (1989).

[53] J. L. Friar *et al.*, Phys. Rev. C **42**, 2310 (1991).

[54] C. Ciofi degli Atti, S. Scopetta, E. Pace and G. Salme, Phys. Rev. C **48**, 968 (1993).

[55] R. W. Schulze and P. U. Sauer, Phys. Rev. C **56** 2293 (1997).

[56] F. Bissey, A. W. Thomas, and I. R. Afnan, Phys. Rev. C **64**, 024004 (2001).

[57] R. W. Schulze, P. U. Sauer, Phys. Rev. C **48**, 38 (1993).

[58] E. Babcock, B. Chann, T. G. Walker, W. C. Chen and T. R. Gentile, Phys. Rev. Lett. **96**, 083003 (2006).

[59] K. D. Bonin, T. G. Walker and W. Happer, Phys. Rev. A **37**, 3270 (1988).

[60] K. P. Coulter, A. B. McDonald, G. D. Cates, W. Happer and T. E. Chupp, Nuc. Inst. and Meth. in Phys. Res. **A276**, 29 (1989).

[61] A. Deninger, W. Heil, E. W. Otten, M. Wolf, R. K. Kremer and A. Simon, Eur. Phys. J. D **38**, 439 (2006).

[62] N. R. Newbury, A. S. Barton, P. Bogorad, G. D. Cates, M. Gatzke, B. Saam, L. Han, R. Holmes, P. A. Souder, J. Xu, and D. Benton, *Laser Polarized Muonic Helium*, Phys. Rev. Lett. **67**, 3219 (1991).

[63] D. J. J. de Lange *et al.*, Nucl. Instr. and Meth. **A 406**, 182 (1998).

[64] D. J. J. de Lange *et al.*, Nucl. Instr. and Meth. **A 412**, 254 (1998).

[65] F. Sauli, Nucl. Instr. and Meth. A **386**, 531 (1997).

[66] B. Ketzer *et al.*, Nucl. Instr. and Meth. A. **535**, 314 (2004).

[67] V. Nelyubin, private communication.

[68] P.V. Degtyarenko, "Applications of the Photonuclear Fragmentation Model to Radiation Protection Problems", Proceedings of the Second Specialist's Meeting on Shielding Aspects of Accelerators, Targets and Irradiation Facilities (SATIF2), 12-13 October 1995, CERN, Geneva, Switzerland, p. 67; P.V. Degtyarenko, M.V. Kossov, H-P. Wellisch, Chiral Invariant Phase Space Event Generator, I. Nucleon-antinucleon annihilation at rest, Eur. Phys. J. A **8**, p. 217 (2000).

[69] D. E. Wiser, Ph.D. Thesis, University of Wisconsin-Madison (1977) (unpublished).

[70] T. Blaich *et al.*, Nucl. Instr. and Meth. **A 314**, 136 (1992).

[71] M. M. Sargsian, arXiv:nucl-th/0110053 and private communication.

[72] J. M. Laget, private communication.

[73] R. L. Jaffe, F. E. Close, R. G. Roberts and G. G. Ross, Phys. Lett. B **134**, 449 (1984).

[74] L. L. Frankfurt and M. I. Strikman, Nucl. Phys. B **250**, 143 (1985).

[75] D. F. Geesaman, K. Saito and A. W. Thomas, Ann. Rev. Nucl. Part. Sci. **45**, 337 (1995).

[76] G. A. Miller and J. R. Smith, arXiv:nucl-th/0107026.

[77] L. L. Frankfurt, G. A. Miller and M. Strikman, Ann. Rev. Nucl. Part. Sci. **44**, 501 (1994).

[78] K. Garrow *et al.*, arXiv:hep-ex/0109027.

[79] B. Hu *et al.*, Phys. Rev. C **73**, (2006) 064004.

[80] S. Dieterich *et al.*, Phys. Lett. B **500**, 47 (2001).

[81] S. Strauch *et al.*, Phys. Rev. Lett. **91**, 052301 (2003).

[82] J. M. Udias, private communication.

[83] J. M. Laget, Phys. Lett. B **273**, 367 (1991).

[84] C. Ciofi degli Atti, E. Pace, G. Salme, Phys. Rev. C **51**, 1108 (1995).

[85] J. Golak it et al., arXiv:nucl-th/0110060.

[86] C. Ciofi degli Atti and L. P. Kaptari, arXiv:nucl-th/0110062.

[87] L. D. Faddeev, *Mathematical Aspects of the Three-Body Problem* (Daniel Davey and Co., Inc., New York, 1965).

[88] R. M. Woloshyn, Nucl. Phys. **A496**, 749 (1989).

[89] G. B. Franklin, `http://www.jlab.org/~franklin/gen/Gen_Asymmetry_Corrections.pdf`

[90] W. Melnitchouk, R. Ent, C. E. Keppel, Phys. Rept. **406**, (2005).

[91] P. Solvignon *et al.*, Phys. Rev. Lett. **101**, 182502 (2008).

[92] M. Amarian *et al.*, Phys. Rev. Lett. **92**, 022301 (2004).

[93] P. L. Anthony *et al.*, Phys. Lett. B **553**, 18 (2003).